CAPITAL UNIVERSITY OF SCIENCE AND TECHNOLOGY, ISLAMABAD

Experimental and Numerical Analysis of Electromagnetic Forming of Al- 6061 Alloy Sheets

by

Faisal Pirandad

A thesis submitted in partial fulfillment for the
degree of Master of Science

in the

Faculty of Engineering

Department of Mechanical Engineering

2021

This thesis is dedicated to my beloved Parents

CERTIFICATE OF APPROVAL

Experimental and Numerical Analysis of Electromagnetic Forming of Al- 6061 Alloy Sheets

by

Faisal Pirandad

Registration No: (MME163012)

THESIS EXAMINING COMMITTEE

S. No.	Examiner	Name	Organization
(a)	External Examiner	Dr. Sohail Akram	PIEAS, Islamabad
(b)	Internal Examiner	Dr. Mohammad Javed Hyder	CUST, Islamabad
(c)	Supervisor	Dr. Salman Sagheer Warsi	CUST, Islamabad

—————————————————

Dr. Salman Sagheer Warsi

Thesis Supervisor

April, 2021

—————————————————   —————————————————

Dr. Muhammad Mahabat Khan   Dr. Imtiaz Ahmad Taj

Head   Dean

Dept. of Mechanical Engineering   Faculty of Engineering

April, 2021   April, 2021

Author's Declaration

I, **Faisal Pirandad ,** hereby state that my MS thesis titled "**Experimental and Numerical Analysis of Electromagnetic Forming of Al- 6061 Alloy Sheets** " is my own work and has not been previously submitted by me anywhere else for taking any degree. At any time if my statement is found to be incorrect even after my graduation, the University has the right to withdraw my MS Degree.

(Faisal Pirandad)

Registration No: (MME163012)

Plagiarism Undertaking

I solemnly declare that research work presented in this thesis titled "**Experimental and Numerical Analysis of Electromagnetic Forming of Al- 6061 Alloy Sheets** " is exclusively my research work with no remarkable contribution from any other individual. Small contribution/help wherever taken has been dully acknowledged and that complete thesis has been written by me.

I understand the zero tolerance policy of the Higher Education Commission and CUST towards plagiarism. Therefore, I as an author of the above titled thesis declare that no part of my thesis has been plagiarized and any material used as reference is properly cited.

I undertake that if I am found guilty of any formal plagiarism in the above titled thesis even after award of MS Degree, the University reserves the right to withdraw/revoke my MS degree and that HEC and the University have the right to publish my name on the HEC/University website on which names of students are placed who submitted plagiarized work.

(Faisal Pirandad)

Registration No: (MME163012)

Acknowledgement

Firstly, I would like to thank ALLAH ALMIGHTY for giving me skills and strengths to carry out all the tasks of this research work successfully. I am deeply grateful to my beloved mother who supported and encouraged me during all this difficult times. She has always prayed for my success in this life and the life hereafter.

I would also like to acknowledge the help and support extended by supervisor **Dr. Salman Sahgeer Warsi**. He tirelessly motivated me throughout the course of this research work with his kind remarks and technical support. It's an honor for me to work under his supervision. May **ALLAH ALMIGHTY** grant countless blessings on him, Ameen. I would also like to thanks **Dr. Waqas Akbar** for his generous support and guidance during this research work.

Thanks also to Ibn e Sina Institute of Technology, Islamabad Pakistan for granting me help in this research work. I would like to express my deepest thanks and gratitude to my friends and research colleagues **Mr. Naveed Hassan Tahir and Muhammad Nazim Sarwar**.

In the end, I would like to thank my siblings for their unconditional and endless love and support.

Faisal Pirandad

Abstract

In the electromagnetic forming (EMF) process, the work piece is deformed at high velocity by the Lorentz force. The cross-sectional shape of the coil, energy levels and capacitance are the three most significant process parameters of the electromagnetic forming process. These parameters govern the spatial distribution of the Lorentz force that causes the deformation of the work piece. The aim of this study is to design a coil for free bulging forming process. The current work investigated both numerically and experimentally the effects of these three parameters on the characteristics of deformed work piece. The characteristics analyzed in this work are Dome height, thickness variation, peak current, deformation profile shape, and the elongation. The workpiece used in this work is AI 6061 aluminum alloy which is widely used in the industry. The widespread use of aluminum alloy can be attributed to its relatively low cost and its properties such as high strength to weight ratio, corrosion resistance, weld-ability, etc. that are better than other alloys of aluminum. The three process parameters analyzed in this research are further sub-divided at three levels. Cross-sectional shapes (circular, square, and rectangle), energy levels (1 kJ, 2 kJ and 3 kJ), and three capacitance levels (2500 μF, 4000 μF and 5500 μF). Full factorial design of experiment is used for experimental design. Three sets of experiments are conducted to enhance the repeatability of the results obtained by the electromagnetic forming process. The elongation of the deformed work piece was measured using the optical microscope. Analysis of Variance (ANOVA) was performed on the experimental results using Minitab software. ANOVA results revealed that energy level is most significant process parameter for Dome height and thickness variation of workpiece. Results showed that maximum displacement is achieved at highest energy level (3 kJ). Square cross-sectional shape and lowest level of capacitance also favorable in achieving high Dome height. Main effect plot result for thickness variation was contrary to that obtained for Dome height. It was observed that lowest possible energy level is best to minimize thickness variation in the workpiece. The analysis of the image of a square region of the specimen using optical microscope showed axial elongation of 7.3% and radial elongation of 6.67%. Comparison of original and deformed

workpiece under SEM revealed that EMF process suppress crack formation. The commercial FEM software (COMSOL V5.6) was used for the development of fully coupled numerical model. The time based solution of the fully coupled model was carried out in COMSOL and validated it with the experimental results. The percentage error between experimental and numerical analysis was found to be less than 5

Contents

Bibliography   77

List of Figures

List of Tables

Abbreviations

CBEP	Capacitor Bank Electrical Parameters
CL	Coil Layers
CMM	Coordinate Measuring Machine
EHF	Electrohydraulic Forming
EM	Electromagnetic
EMC	Electric-Magnetic Coupled
EMF	Electromagnetic Forming
EMMC	Electric-Magnetic-Mechanical Coupled
EMPW	Electromechanical Properties of Workpiece
FEA	Finite Element Analysis
FLD	Forming Limit Diagram
HERF	High-Energy-Rate Forming
HVF	High-Velocity Forming
MMC	Mechanical Magnetic Coupled
NC	Non Coupling

Symbols

$\mathbf{R}_c$	Resistance of Coil
$\mathbf{R}_O$	Capacitor Bank Resistance
$\mathbf{RLC}$	Resistence Inductance Capacitor
$\mathbf{A}_c$	Cross-section Area of Coil
$\mathbf{A}_s$	Analytical Solution
$\mathbf{C}_G$	Geometry of Coil
$\mathbf{E}$	Electric Field
$\mathbf{E}$	Young's Modulus
$\mathbf{F}$	Flat coil
$\mathbf{H}$	Magnetic Field Intensity
$\mathbf{L}_c$	Inductance of Coil
$\mathbf{L}_O$	Capacitor Bank Inductance
$\mathbf{L}_s$	Inductance of Electric Circuit
$\mathbf{N}_s$	Numerical Solution
$\mathbf{N}$	No of Turns
$\mathbf{R}_i$	Spiral Coil Inner Radius
$\mathbf{R}_o$	Spiral Coil Outer Radius
$\mathbf{R}_r$	Radial coil
$\mathbf{R}_w$	Electrical Resistivity of Work picec
$\mathbf{V}_m$	Maximum Voltage
$\mathbf{V}_o$	Discharge Voltage
$\mathbf{W}_G$	Geometry of Workpiece
$\mathbf{R}_e$	Resistance of Electric Circuit

Chapter 1

Introduction

1.1 Sheet Metalworking

Sheet metalworking is the process that involves cutting and forming operations performed on thin metal sheets [1]. This process is capable of producing products that are geometrically precise, of high quality and are ready to use. Sheet metalworking is one of the most widely used manufacturing process in industry [2]. The commercial importance of sheet metalworking can be gauged by the considering the number of industrial and consumer products that employ sheet metal components. These products vary from aerospace and automobiles to consumer electronics to furniture. Sheet metalworking has a special importance in automobile industry, owing to its ability to form thin walled yet high strength machine components. This aspect of sheet metal forming is particularly important from viewpoint of weight reduction of automobiles that leads to enhanced fuel efficiency [3].

Conventional sheet metal working is done on machine tools called presses (often called as impressing press). Punch-and-die is the tooling that are used in conventional sheet metalworking operations such as cutting, bending and drawing. The development of die-and-punch involves considerable design efforts and significant cost. This cost of tooling is then translated into the final cost of the finished product. However, the cost of the finished product can be optimized by producing parts in large quantities [4]. In addition to the sheet metalworking operations

performed on the stamping presses, there are other sheet-metal operations that do not require conventional stamping presses. Such processes include, spinning, stretch forming and high energy forming. One of the advantage of such processes is near-elimination of die and punch cost. Regardless of the type of sheet metalworking process used, the aspect of formability of workpiece material is of paramount importance.

1.2   Formability

Formability is the characteristics of a workpiece to undergo permanent deformation. Plastic deformation is the continuous distortion that happens when a material is subjected to compressive, bending, stresses of tensile or torsion that exceed its yield strength and cause it to compress, stretch, elongate, buckle, or twist. Formability relies on a material's properties and also on the phase parameter of the forming activity [5]. For sheet metal forming, the typically quasi-static method is used. A punch, a die and a set of blank holders are the basic components of traditional shaping. To form the appropriate shape, the punch draws the primarily flat blank into the die opening. Failure in the molded parts is caused mostly by either wrinkling or tearing. The excessive compressive and tensile stresses in the plane of the sheet are created by bulking and tearing during the forming process [3]. Due to the tooling geometry and the friction, the deformation is inhomogeneous during sheet metal forming. In multiple areas, the pressure states and stress states are different. Sheet metal's low formability is also a problem for the traditional forming process.

In conventional forming process, usually two methods are used to achieve the desired deformation. One is to regulate the distribution of strain and the other is to enhance the mechanical properties of the material. Several processing techniques, such as lubrication and blank holder power, have been developed to regulate the distribution of pressure [6][7]. However, there are disadvantages of conventional forming such as wrinkling, tearing, requirement of lubrication, spring back effect, bulking and slow processing. The concept of limit forming is generally used to describe the amount of plastic deformation that can be imposed before the sheet

material breaks. However, with traditional forming methods, the tendency of metals to neck and tear at rather low strain levels makes them difficult to use for producing geometrically complex pieces. At high strain rates, the formation limit of many materials increases[8].

1.3 High-Velocity Forming (HVF)

High-Velocity Formation (HVF) can lead to increased ductility, with a much higher strain rate in the neck than the rest of the sample. If the strain rate of the critical material neck area is diffused, the materials may be hardened [12]. In the experimental and numerical analyses of HVF, inertia effect on tensile ductility is positive, high-speed formation has been demonstrated. This is in contrast to the quasi-static system where formability limits the overall process.

HVF processes rapidly transfers energy to workpiece over short periods of time. The acquired kinetic energy is change in plastic work during metal deformation, thus the workpiece is rapidly covered distance away from the energy source. High forming speeds are obtained, usually ranging from 50-300 m/s. The magnitude and time of pressure application is the aspect that distinguishes the HVF methods from traditional metalworking procedures. Physics is very distinct under complex shaping conditions, and inertia is an important factor. Inertia is ignored in traditional forming circumstances as the forming velocity is usually less than 6 m/s. Typical velocity-speed formation operations are conducted at sheet speeds of about 100 m/s [13].

In the automotive industry, there is considerable interest in the manufacture of body parts and panels with aluminum or thin steel sheets of high strength, taking into account the key advantages of weight savings and corresponding fuel consumption. As a result, interest in HVF is renewed. All the techniques of HVF lead to established formability, improved distribution of strain, wrinkling reduction, spring back control, and interference between the workpiece and the specific die. This is in adding to other commercial advantages, such as lighter tools and supplies and short processing times.

1.4 Types of HVF

Dependent on the source of energy, there are many HVF methods. Electrohydraulic formation, gun forming, explosive forming, and electromagnetic forming are typical methods. These are all similar in the sense that at the beginning of the process, the workpiece acquires kinetic energy and then largely deforms due to the inertial effect.

1.4.1 Explosive Forming

One of the techniques for forming metal plate into a cavity is by using high shock pressure from the explosive charge. An explosive easily releases its energy such that at the moment of the explosion an extremely high pressure for a limited duration occurs. If the metal plate is struck by an underwater shock wave, the metal plate is instantly accelerated at a high velocity to collide with the die.

1.4.2 Electrohydraulic Forming

Electrohydraulic forming (EHF) is ultra-high-velocity metal deformation using water shock wave developed by electric energy discharged from two electrodes submerged in fluid. However, this process is only ideal for smaller works, and the need for vacuum makes the equipment more difficult to handle.

1.4.3 Electromagnetic Forming (EMF)

Electromagnetic forming (EMF) is one of the smartest high-speed forming process in the commercial metal forming industry, which has become increasingly popular. Huge forces can be conveyed to a workpiece through pure EM interference in this non-contact technique. A keen interest in the EMF process was established between 1960 and 1970. Early literature has provided valuable information about the EMF mechanism. However, owing to a lack of high-performance materials and equipment, this technique was not studied extensively as an application in the industry. EMF method is an extremely simple, single-step procedure. The

workpiece is deformed in microseconds at the rate of 200-300 m during the EMF process. Wrinkling is suppressed because of high-speed formation. Furthermore, reduction in spring back as well as high productivity are other prominent benefits [13]. The Electromagnetic forming method for forming of Al 6061-T6 sheet has been extensively investigated in the present research.

1.4.3.1 Application of EMF

The EMF method is capable of an extensive variety of forming, such as bulging of thin tubes and bulging of tubes into complex shapes. It has found widespread application in the manufacture of asymmetrical, circular and axisymmetric shapes.

1.4.3.2 Principle of Electromagnetic Forming (EMF)

A strong temporary current flows through the coil in the electromagnetic forming phase when the capacitor bank is discharged, and a time-varying magnetic field is generated around the coil. An electric current will flow in a conductor (metallic workpiece) that is connected to a changing magnetic flux according to Faraday's law of induction. The induced current can flow in the opposite direction with respect of the coil current under Lenz law. A repulsive force is created between the sheet and the actuator coil and as a consequence, the workpiece is deformed with high velocity.
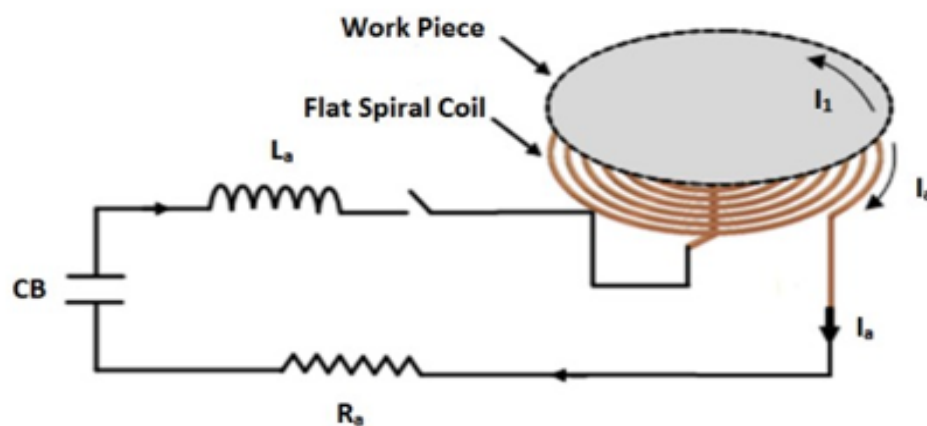
FIGURE 1.1: Schematic Diagram of EMF [14]

1.4.3.3   Types of EMF Process

There are typically two types of EMF processes, i.e., radial solenoid coil, and straight circular coil which are divided according to geometry. The new implementation of the EMF technique has also appeared recently, such as electromagnetic penetration, [15], joining the metal [16] and welding[17]. By using the solenoid coil, compression, radial deformation and expansion are produced. For the sheet metal formation, the flat spiral actuator coil is used. The EMF is a modern sheet metal-forming technology.

1.4.3.4   EMF Process Parameter

The formation of EMF sheets depends on many process parameters, such as actuator coil cross-section area, capacitor bank capacitance, capacitor bank energy, the spiral coil cross-section shape, discharge voltage, the gap between the work sheet and the actuator coil. If the capacitance of the capacitor bank is too high or too small, it directly influences the axial distortion[18]. Extensive research has been done in literature to assess the effect of factors, such as lubrication, discharge voltage, blank holder power and the two-step EMF process. Decreasing the force of the blank holder and the increasing lubrication results in an increase in the height of deformation [19]. The effect of spring back effect in electromagnetic-assisted bending of aluminum alloy sheets has also been studied in literature [20]. The results of the study showed that spring back action is considerably reduced in EMF process. The actuator coil is generally constructed according to the required shape for uniform electromagnetic strain.

Electromagnetic formation can be used to modified a range of parts very effectively, such as fuel cell panels, mobile phone cases, car door pockets, etc.[21]. An analytical equation to estimate the stress distribution in EM sheet forming process using a flat spiral coil was presented in [22]. Another study formulated the relation between mechanical and magnetic phenomena, and proposed a fully coupled model that also acknowledged the effect of a workpiece displacement velocity on the development of the magnetic field [23]. The study also provided the experimental and numerical results for the performance evaluation of the proposed Daehn and

Fenton model. CALE simulation software was used to model and simulate the EMF mechanism [24]. The ADINA program was used in another research that investigated the EMF process to calculate free bulging of sheets [25]. Without even realizing the stress distribution in the constitutive equation of the material in the mechanical fault, both works reached a results with the experimental deformation shape production [13]. Past researchers have also established a non-coupled method to solve mechanical and magnetic problems using commercial FE codes [26]. For the calculation of the electromagnetic force the analytical equations are presented [27]. The impact of workpiece movement on the inductance was ignored in both works, and an evaluation was made of the magnetic force density distribution within the workpiece and the magnetic field [28]. The frequency of discharge plays an significant role in the workpiece deformation. But optimizing the current frequency according to sheet thickness is very difficult task. The width of the skin is still less than the sheet thickness [29]. The uniform magnetic field relies on the actuator coil's geometry.

1.5 Problem Statement

From the previous discussion, it is evident that the most important factor in EM sheet forming is capacitance (μF), discharge energy (kJ), the cross-section shape of the actuator coil. In order to fully understand and optimize EMF process, an in-depth analysis of the effect of the aforementioned factors is of paramount importance. Therefore, the present work is aimed at investigating the effect of cross-section area, capacitance, discharge energy on the deformation of workpiece. The thickness distribution of deformed workpiece was also compared with the numerical result.

1.6 Research Methodology

The methodology used in this work has two parts, experimental work, and numerical work. Experimental part consist of design of experiments, and statistical

analysis of experimental data. Numerical part of methodology consists of model development, model discretization, and simulations in COMSOL multi-physics for EMF process. The results from numerical model have been validated with experimental results. **Figure 1.2** presents an overview of the methodology used in this research.
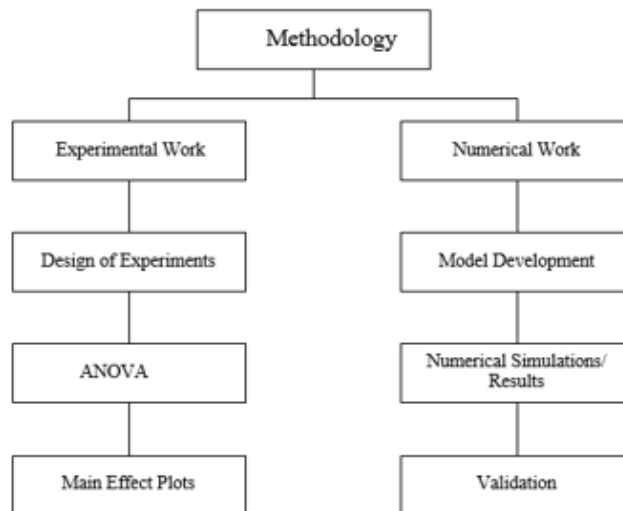
FIGURE 1.2: Methodology used in this Work

1.7   Organization

Chapter 1 presented a brief introduction of the problem studied in this research. Chapter 2 presents an updated review of the literature done related to EMF process. Chapter 3 presents in detail the methodology used in this research. It elucidates the experimental and numerical methods used in this research. Chapter 4 describes an in-depth statistical analysis of the experimental data. Numerical methods employed in this research are presented in Chapter. Conclusions and further research directions are presented in Chapter 6.

Chapter 2

Literature Review

This chapter presents a detailed review of notable and highly cited studies performed for EMF processes. The literature presented in this chapter can be broadly divided into two categories, namely: experimental and numerical studies.

2.1   Experimental Studies

Pioneering work on the mechanism of electromagnetic formation was done by Al-Hassani et al. [22]. The authors studied the expansion of aluminum (Al 1471) tube having wall thickness 0.064 in and a diameter of 2 in. EMF process was performed with an energy of 1.5 kJ. Field shaper was placed between coil and workpiece to perforate workpiece as shown in **Figure 2.1**. The authors also developed approximate equations to describe the EMF process. Their results showed EMF to be a promising technique that can be used for a variety of forming shapes in the future.

Takatsu et al. [23] investigated the electromagnetic free bulging of aluminum circular sheets. For EMF tests, a single-layered 5 turn flat spiral coil was used. The spiral coil, Capacitor bank, and aluminum sheet parameters used in the study are presented in **Table 2.1**. The high-speed camera was used for measuring the formation phase. Deformation was observed to start 19 μS after the capacitor bank was discharged. The deformation was captured by a high-speed camera, which began at a distance of 20 mm from the middle of the aluminum sheet. The
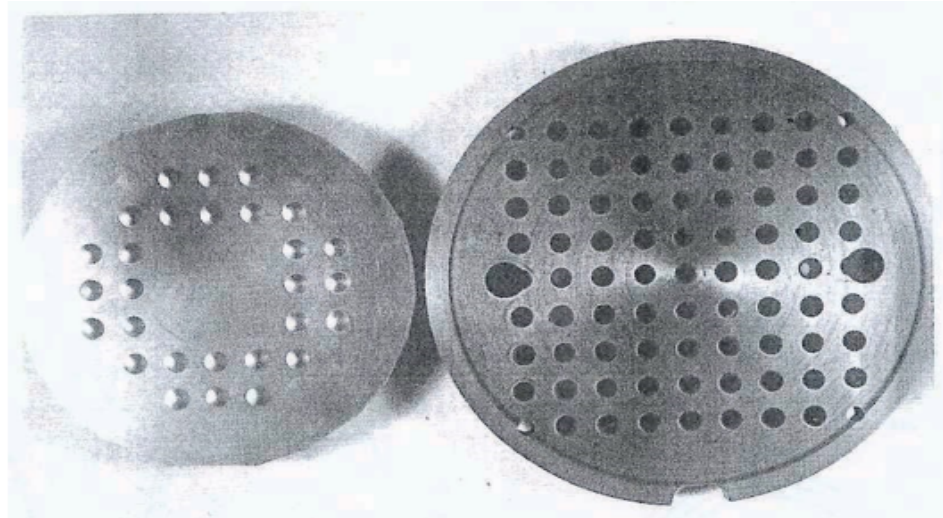
FIGURE 2.1: Deformed Work Piece with Forming Die and dimples [22]

entire process of formation was completed in 250 μS. The progression of forming during the entire process, as captured by the high-speed camera is given in **Figure 2.2**.

TABLE 2.1: Parameters of Coil, Capacitor Bank, and Work Piece [23]

Component	Parameters	Specifications
Coil	Material	Copper
	No of turns (N)	5
	Maximum Radius of coil	32mm
	Self-Inductance (L1)	0.86 μH
	Pitch (Pc)	5.5 mm
	Wire diameter (d)	1.6 mm
Capacitor Bank	Capacitance Co	40 μF
	Discharge Voltage Vo	6.0 kV
	Circuit Inductance	2.0 μH
	Circuit resistance	25.5 mW
Work Piece	Material	Aluminum (Annealed)
	Diameter	110 mm
	Thickness	0.5 mm
	Gap distance	1.6 mm

It can be seen from **Figure 2.1** that the deformation began away from the middle of the worksheet. The results of the study showed that the magnetic field variation obtained by the flat spiral coil is non-uniform.
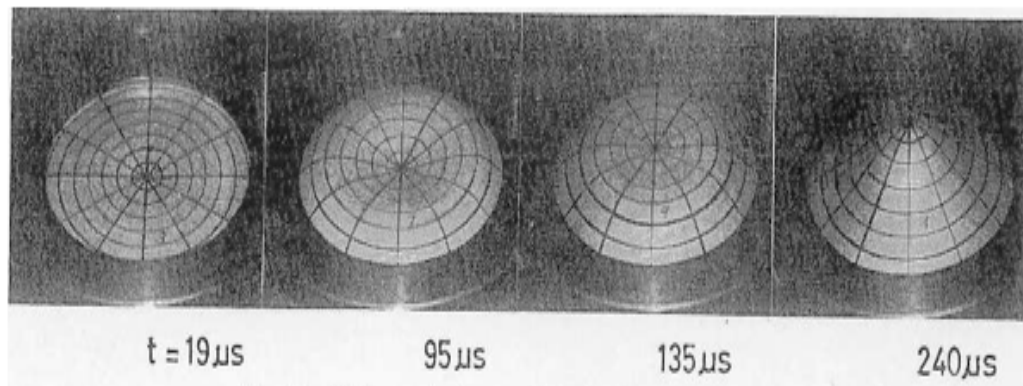
FIGURE 2.2: Deformation of Work Piece with Respect to Time [23]

Imbert et al. [30] presented an analysis of the effect of tool-workpiece contact on damage evolution in EMF in aluminum alloys. For this analysis, two methods were implemented. Free bulging and specific tapering die deform of 1 mm thick sheet aluminum industrial alloys (AA5754) were used for experiments. Capacitor banks with a storage capacity at 15 kV of 22.5 kJ, a system of the capacitance of 200 μF and inductance of 230nH were used for research. A smooth seven-turn twisting coil with a diameter of 120 mm was used. In order to prevent tearing in the free fabrication process, the die entry radius was 10 mm and a tapering die with a height of 38 mm was used. A small increase in workpiece formability in the free bulging, and otherwise a significant increase in workpiece hardness by using coNIcal die was observed. High strains beyond the traditional forming limit diagram (FLD) were experiential in a narrow area in free bulging studies. The same high strains were observed in a wider area in tapering die experimentations. Figure 2.3 shows the deformations observed in the part in this study. The results of the study showed that tool-sheet interaction is critical for damage evolution. These findings were further substantiated by metallographic analysis.
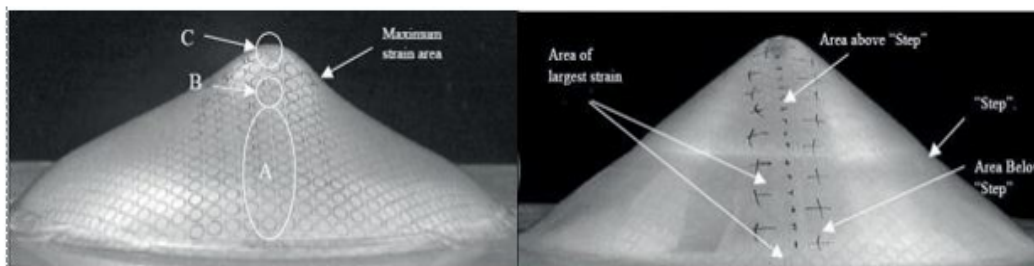
FIGURE 2.3: Free Forming and Conical Die Forming [30]

Thus, it was concluded that the forming limit of the aluminum sheet improves during the EMF phase because of the interaction of the tool and sheet. An increase at the top of the workpiece during the discharge energy in the free forming process was observed as shown in **Figure 2.4**.
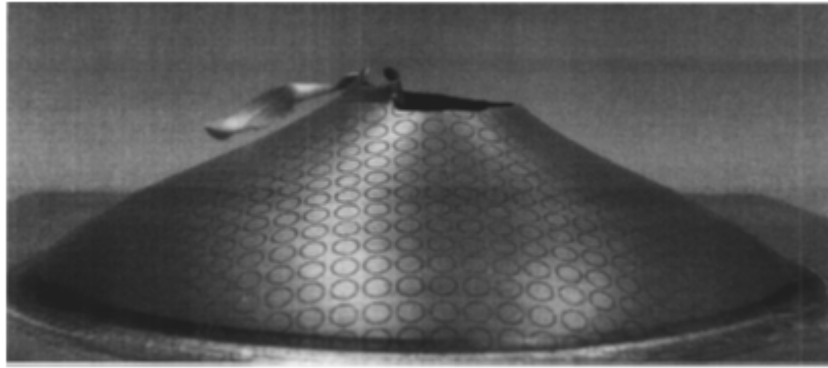
FIGURE 2.4: Neck Fracture of Aluminum Sheet at High Energy Level [30]

Padmanabhan [31] investigated both sheet formation and tube forming. Aluminum and copper wrinkling and spring-back properties in EMF sheet metal formation and electromagnetic tension of ring were studied. Numerous material and process variables were varied and their effects were analyzed on twisting and spring-back. A spiral actuator coil was used to carry out the sheet metal EMF experiments. The research analyzed the energy impact of the EMF process on (AL-1100-O), sheet metal thickness, metal temperature (T6 tempered and O tempered), die geometry, coil and sheet gap, and content (Oxygen Free High Conductivity copper and Al 1100-O aluminum). For the spring-back measurements, CMM was used.

A small range of EMF process implementations and capabilities were demonstrated. The maximum charging capacity of the capacitor bank was 50 kJ. The generator consisted of eight 10 μF capacitance capacitors for each capacitor. The research work was carried out using four 640 V-charged capacitors. Deformed workpiece at different energy level is shown in Figure 2.5 [31]. It was concluded that wrinkles are reduced by enhancing the capacitor bank's discharge energy, and wrinkles decrease at the specified point of discharge energy as the sheet thickness enhances.
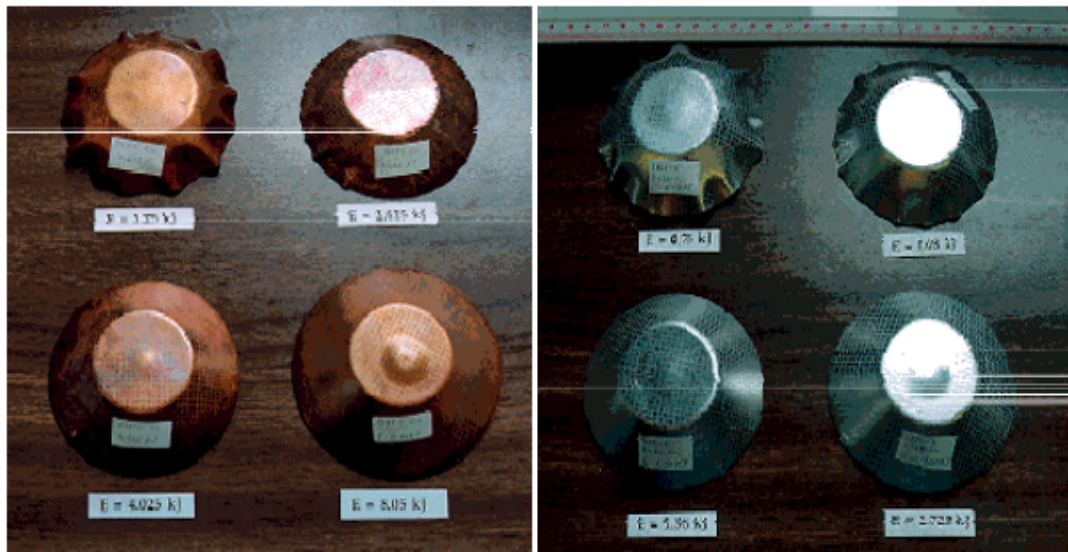
FIGURE 2.5: Copper Samples and Aluminum Samples [31]

Seth et al. [9] explored the formability of cold-turned sheet steel at high velocity as formed with a rounded knock effect. The impact of velocity evaluations was found with the aid of a high-speed camera. It was observed that the samples' impact velocity improved almost linearly with the launch energy.

A commercial capacitor bank for Maxwell-Magneform was used. Total eight capacitors, 120 μF each, linked in parallel, were included. If the maximum charged voltage is 10kV, the bank's total energy was 48 kJ. Just four of the eight capacitors were linked in this study. Hence, the bank's maximum available discharge capacity was 24 kJ.

The charging voltage was wide-ranging to regulate the energy of the discharge. For the wrapping of a four-turn single layer flat actuator coil, a square cross-section of copper wire (5.3 mm) was used. It was embedded in the adhesive with a Kevlar face sheet for coil strength. The outer diameter of the spiral was 83 mm, a height of 24 mm over all the dimensions of the actuator coil block, and an outer diameter of 127 mm.

The 6 mm gap between the actuator coil and the piece of work was retained. The 80 mm diameter workpiece and the electrolytically polished with a 2.54 mm circle were used [9]. Examples of deformed workpieces are shown in **Figure 2.6**.
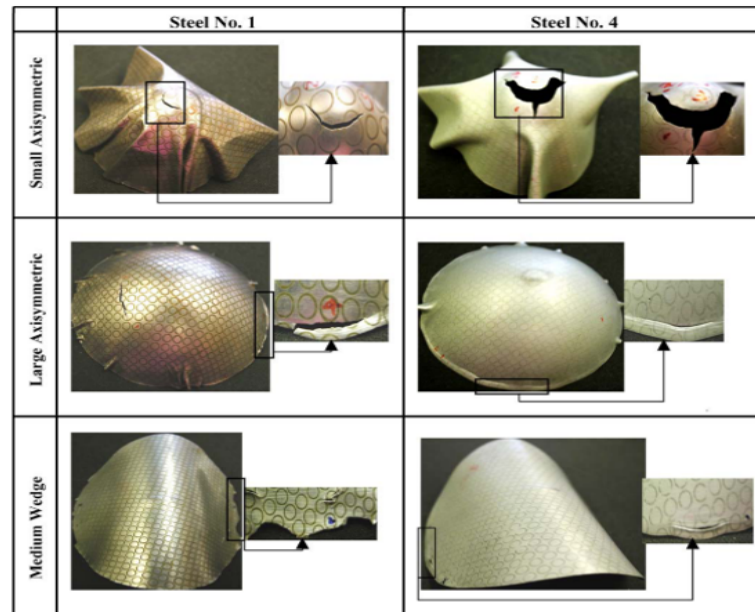
FIGURE 2.6: Observed Failure Modes [9].

The experimental investigation was performed using industrial Aluminum Alloy 1, 1 mm (AA 5182 and 1.6 mm AA 5754) by Oliveira et al. [32]. As predicted from the forming limits diagram, the weakness of strains of all the steels were increased significantly beyond those examined in tensile tests. The impact of die geometry is studied on formability, strain state, and failure position [32]. In the G-10 Garolite insulator, which is protected by a thin layer of epoxy, a single layer of the double rectangular spiral coil was incorporated which is shown in **figure 2.7**.
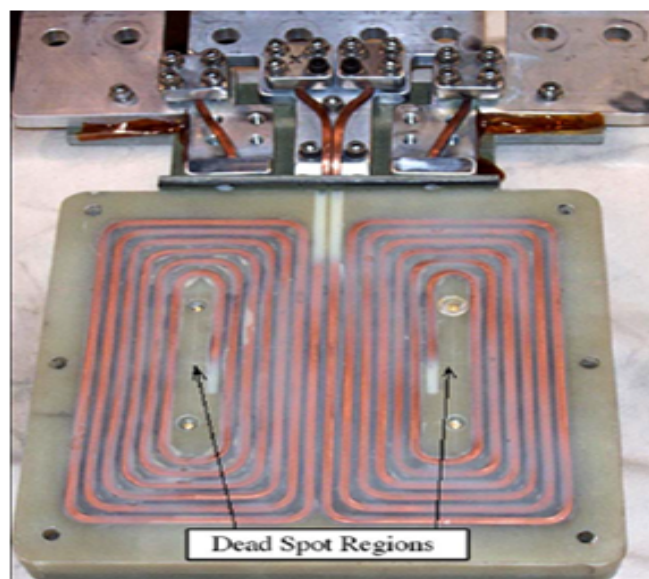
FIGURE 2.7: Double Spiral Coil [32]

The studies were conducted out using a 4.8 to 16.9 kJ power supply range, with a 5-6 kHz current-discharge frequency. Device capacitance 600 μF, total inductance 1.61 μH, coil resistivity 1.7 e-8 Ω/m, system inductance 50 nH, strain rates 2000-3000S-1, charging voltages (V0) 4-7.5 kV, cables inductance 160 nH and air distance between workpiece 3.175 mm were the circuit parameters and system [32]. Mathematical modeling and measurement methodology of thin round sheets using a flat spiral actuator coil for EMF was focused on by Paese et al. [33].

The methods were based on the Biot-Savart Law that measures and evaluates the electromagnetic field generated by the spiral actuator coil before the sheet's plastic deformation. In order to verify a successful relationship with the mathematical model, free bulging experiments were carried out. For experimental work, 3.4 kJ maximum capacitor bank energy, an actuator coil of outside diameter 120 mm, the capacitance of 8400 μF, number of turns 6, maximum voltage 900V, and cross-section area 16 mm2 was used. For the EMF process, commercial aluminum alloys with different sheet thicknesses (0.3, 0.5, and 1) mm were used. The experimental results are presented with different thickness in **figure 2.8**.

FIGURE 2.8: Experimental Work with Different Thickness [33]

Similarly, a method for measuring the electromagnetic force in aluminum sheet Al 1050 using a flat spiral actuator coil was demonstrated by Paese et al. [34]. The approach was based upon the law of Biot-Savart. On commercial electromagnetic forming machine SMU1500, free bulging tests were performed. A single layer 6 turns flat spiral actuator coil outer diameter 66.25 mm, self-inductance 0.92 μH with 5.5 mm pitch between the coils turns and coil cross-section area 20 mm2. The capacitance of the capacitor bank was 60 μF and 1.5 kJ maximum discharge energy. Experiments were performed on different energy levels (500 J, 800 J, and 1000 J). The result of free bulging experiments on different energy levels is shown in **figure 2.9** [34].

FIGURE 2.9: Free Forming at Different Energy Levels [34]

Modeling, experiments, and evaluation were part of a recent report on the electromagnetic formation (EMF) [35]. In a capacitor bank SMU 1500 EMF unit, free bulging of aluminum sheet metals was carried out. For the EMF-free formation process, a flat actuator rectangular spiral coil was used. The parameters of the capacitor bank, coil, and aluminum sheet are given in **Table 2.2**.

TABLE 2.2: Parameters of Coil, Capacitor Bank, and Work Piece [35]

Component	Parameters	Specifications
Coil	Material	Copper
	No of turns (N)	6
	Maximum Radius of coil	32.5mm
	Self-Inductance (L1)	0.9 μH
	Pitch (Pc)	5.5 mm
	Cross-section area (Aa)	20 mm2
	Resistance (Ra)	0.6m Ω
	Cross-section size	(2.5, 8)mm
Capacitor bank	Capacitance Co	60 μF
	Discharge Voltage Vo	7.1 KV
	Maximum Energy	1500J
Work piece	Material	Aluminum A1050 (Annealed)
		110 mm
	Diameter	1 mm
	Thickness	2.5 mm
	Gap distance	12.5 kN
	Blank holder force	

A check coil was used to calculate the induced current without the workpiece in the actuator coil. EMF free-forming experiments with the same thickness and the same substance were carried out at various energy levels. At the energy level of

500 J, the Dome height was estimated at 19 mm and at the highest level of 1820 J, which was 40 mm. However, a dimple on the top surface of the dome nipple was found. The total workpiece was deformed at the level of 1500 J at a height of 39 mm [35]. Different photographs of the deformed workpiece are shown in **Figure 2.10**.
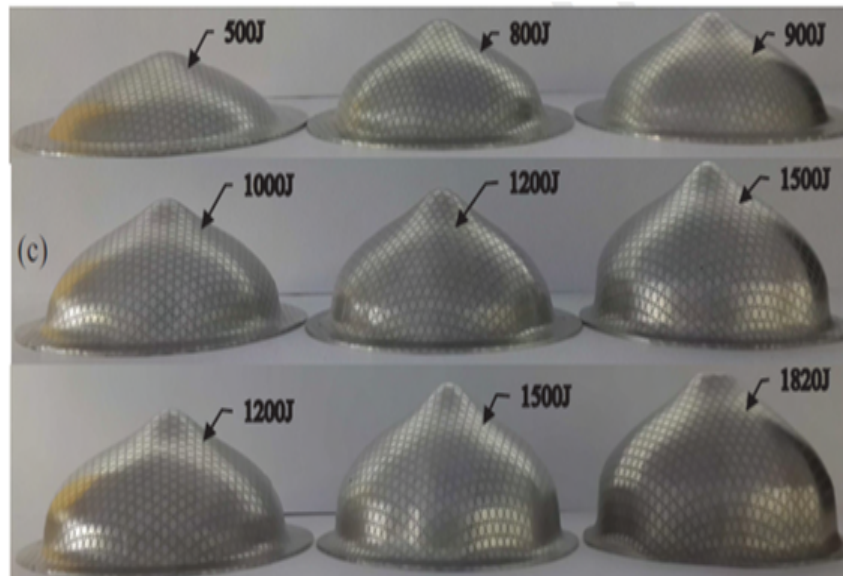
FIGURE 2.10: Deformed Work Piece at Different Energy Levels [35]

2.2   Numerical Modelling and Simulation

Due to the state of coordinated simulation of interrelated mechanical, electromagnetic and thermal phenomena, the EMF is a difficult job to numerically simulate. In the past, researchers and scientists were not able to model these extremely complicated methods correctly. More and more research for the simulation of the EMF method has been carried out alongside the advancement in the computation area. The EMF approach is regularly used as a mixture of two primary body phenomena, the physics problems and specifically EMF issues. As previously discussed, these two problems are usually inter-related due to the resilient influence on the deformation of the workpiece of the parameters of the circuit. In the EMF theory, mechanical problems are tested in several respects and the simulation of mixed EMF [36]. Three methods have been developed for numerical modeling the EMF

method. This method depends on the electromagnetic issues and the dynamics. The second is the loose coupling between the EM and the solid mechanics, and the third is the fully coupled electromagnetic and magnetic coupling of the mechanical and electromagnetic problems. These techniques are further discussed in detail.

2.2.1 Non-Coupling Technique

The non-coupled method is the easiest one. Maxwell's equation is given with the behavior of the job deformation taken into consideration. The Lorentz force was first measured from the electromagnetic circuit in the non-coupling technique and then transferred the Lorentz force to the solid mechanics as the data of input induced by the distortion of the work object. In early 1970, a study on EM numerical simulation provided the state of the art. Due to different coils on flat sheets, the magnetic field distribution was analytically determined. No simple geometries were examined for the strength of the magnetic field and magnetic pressure bent by the twisting coil. For the flat curved coil measuring the magnetic pressure, **equation 2.1** is given below [22].

$$P_r = \frac{\mu_o I^2 N^2}{2\pi^2} \left\{ \ an^{-1} \left[\frac{-2gr}{g^2+a_2^2-r^2} \right] + tan^{-1} \left[\frac{-2gr}{g^2+a_2^2-r^2} \right] \ \right\}^2 \tag{2.1}$$
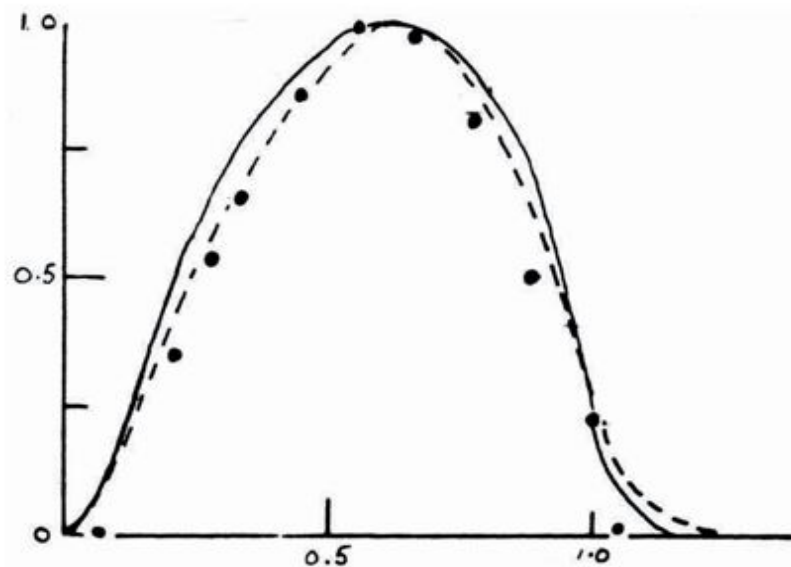
FIGURE 2.11: Numerically Magnetic Pressure Distribution [22]

Discharge current is the I, the number of turns of the flat coil are represented by N, G is the gap of the workpiece and the coil, a1 is the displacement from the midpoint of 1st turn, a2 is the displacement from the midpoint of the last turn of the coil. Al-Hassani compared the analytical result with experimental work done shown in figure 2.11. It was found that the analytically obtained magnetic pressure was in strong agreement with the experimental findings.

The mechanism of the EMF has been studied analytically by different researchers [37] [38]. These theoretical studies are based on basic axisymmetric configurations, compression of the tubes, and expansion of the ring [38]. EMF equipment is designed as an electronic circuit counterpart. To achieve the current in the capacitor bank and coil as a primary circuit and the workpiece as a secondary circuit, a partial differential equation with respect to time must be solved in a sequence of two first order. Finite element model is a perfect tool for a few years to determine the mechanical response of materials, with an enhancement in the calculation capability of the machine. Within the context of the non-coupled methodology, Imbert et al. [30] performed a numerical study of the EMF workpiec test.

The purpose of the work was to determine that the forming ability of aluminum alloy sheets that is enhanced by the EMF process. The numerical simulation was conducted using the viable dynamic analysis FEMM code LS-DYNA [39]. The material damage conduct was formed with the Gurson-Tvergaard-Needleman constitutive model, which consists of the Gurson Yield function, with the modification proposed by Tvergaard and Needleman. For its ability to study the evolution of ductile failure and damage, this type of model has been extensively selected by past researchers [40] [41] [42]. As small rate sensitivity is present in the aluminum alloys tested, the plastic nature of the material is characterized by isotropic rate-independent stiffening regulations.

2.2.2   Loosely-Coupling Technique

The generated Lorentz forces are calculated using the electromagnetic model at each point of the time increase in the loosely coupling technique. As an input load, the pressures are then passed automatically into the mechanical model. The

new geometry updated by the solid mechanics model is used to calculate the electromagnetic flux for the further steps. This approach is replicated sequentially till the completion. This technique is used to gives a precise result with a low computational effort. However, in this technique loosely coupled system having some assumption, adiabatic process, neglected the thermal effect. The relation between the EM and the mechanical model is shown in **Figure 2.12**.
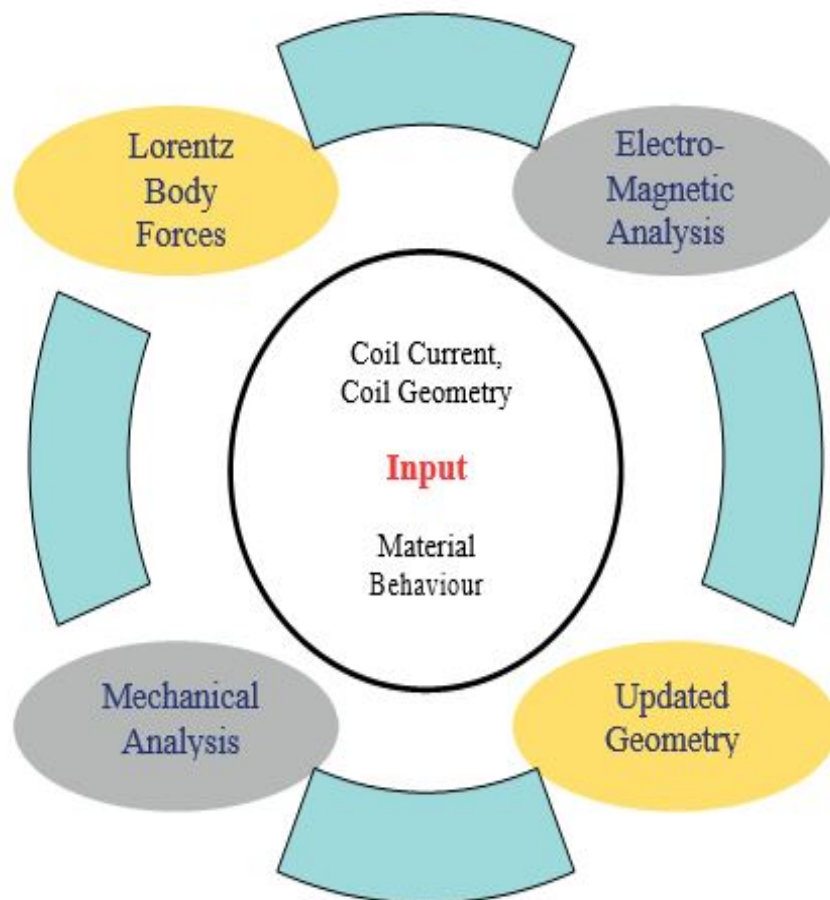
FIGURE 2.12: Loosely Coupling Technique. [43]

In early work, the fundamental equations to solve the EM open die sheet forming were described by the electromagnetic field, circuit analysis, and dynamic equations of the permanent deformation of the sheet. An axisymmetrical configuration for the numerical solution was used for both the coil and the workpiece [23]. Afterward, the workpiece is placed on the spiral coil and hold with the help of a blank holder. The mathematical simulations and experimental responses developed for preliminary validation are discussed in **Figure 2.13**.
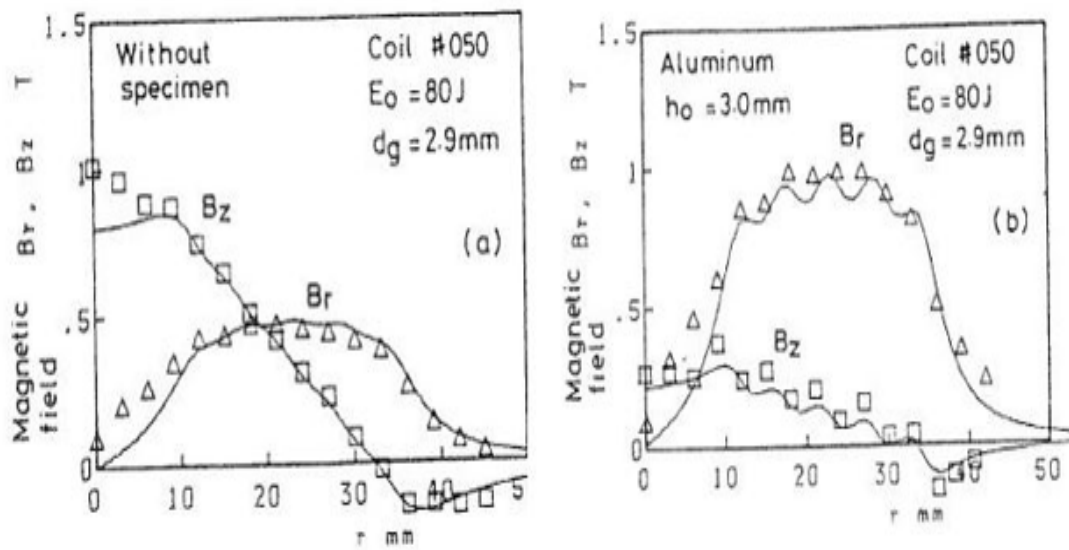
FIGURE 2.13: Distribution of Magnetic Field with and without a Fixed sheet in radial. [23]

The points scattered are experimental findings, while the numerical figures are straight lines. As the sheet is mounted on the coil, the radial portion of the magnetic field is substantially enhanced in **Figure 2.13 (b)**. In the induced currents, the shape shift of the workpiece and rate sensitivity were taken into account, but the impacts of bending and temperature were ignored. The numerical findings are in strong agreement with their experimental result are shown in **Figure 2.14**.
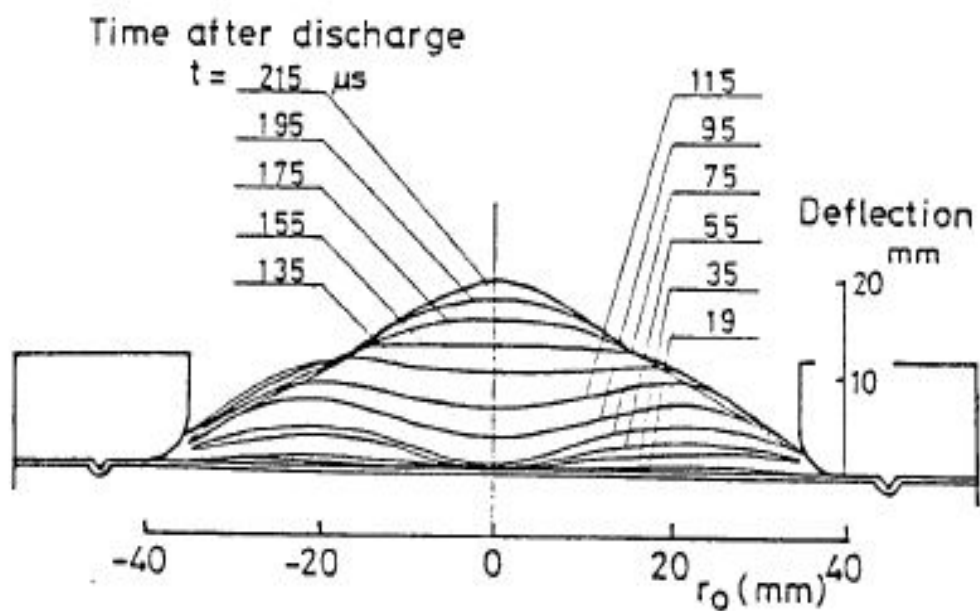
FIGURE 2.14: Deformation Profile of Sheet [23]

2.2.3 Fully-Coupled Technique

The key downside of this approach is the difficulty to compute the electromagnetic and solid mechanics model so that the computational cost is too high. With the aid of the CALE code, researchers developed a bi-dimensional FE model, a fully electromagnetic-mechanical coupled model. Fenton and Daehn used a hardening law independent of the reactivity of the strain rate [24]. Table 2.3 presents the researched work of the EMF method, inputs, analysis and model was validated and/or checked chronologically. **Table 2.4** takes into account the detailed coil parameters (electrical and geometrical) and the capacitor bank.
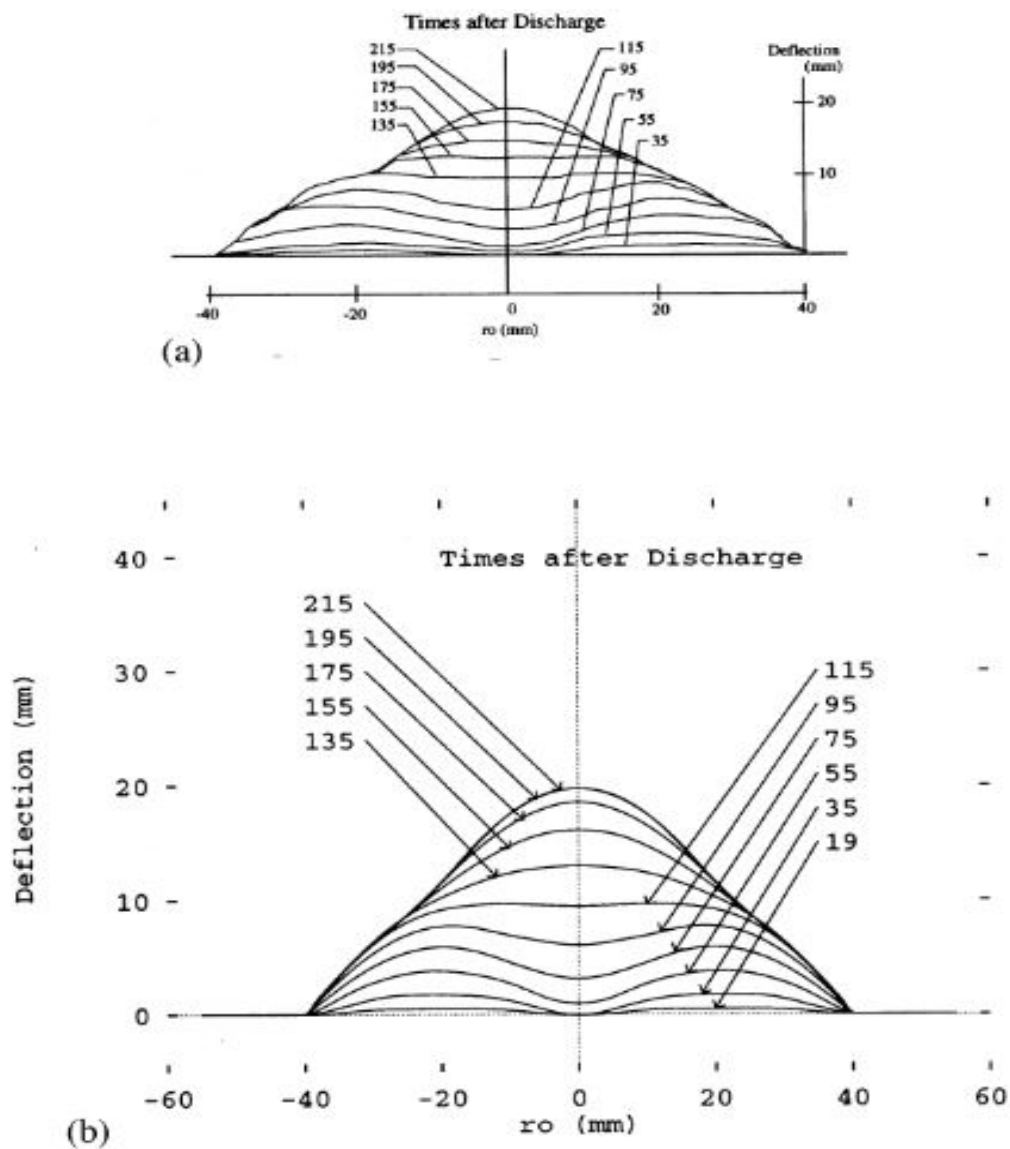
FIGURE 2.15: Deformed Profile (a) [23] and (b)[24]

TABLE 2.3: Techniques of Required Inputs, Study, and Outcomes

Reference	Method of	Necessary inputs	Out comes
[22]	NC and As	CG and DC	Comparison between Self Experiments and Analytically Outcomes
[23]	Ns with MMC	CBEP, WG, CG and DC	Comparison between Self Experiments and Analytically Outcomes
[24]	Ns with MMC	CBEP, WG,CG, DC and EMPW	Comparison of the numerical outcomes
[44]	Ns with MMC	CBEP, WG,CG and EMPW	Only numerical Outcomes
[32]	Ns with MMC	CBEP, WG,CG, DC and EMPW	Comparison between Self Experiments and Analytically Outcomes
[45]	Ns with MC	WG,CG, DC and EMPW	Only numerical Outcomes
[47]	Ns and NC	WG,CG, DC and EMPW	Comparison of the self experiments and the numerical outcomes.
[25]	Ns with MMC	WG,CG, DC and EMPW	Comparison of the self experiments and the numerical outcomes.
[27]	As and NC	WG,CG, DC and EMPW	Comparison of the outcomes of analytical formulations with the other researchers work
[48]	NC and Ns	CBEP, WG,CG, DC and EMPW	Comparison of the self experiments and the numerical outcomes.
[49]	Ns with EMC	CBEP, WG,CG, DC and EMPW	Comparison of the self experiments and the numerical outcomes.
[50]	NC and Ns	CBEP, WG,CG, DC and EMPW	Comparison of the self experiments and the numerical outcomes.
[51]	Ns with EMMC	CG, CBEP , WG and EMPW	Comparison of the self experiments and the numerical outcomes.

TABLE 2.4: Specification of The Energy Source and Flat Spiral Coil

	Flat spiral coil					**Energy Source**					
Reference	Ri	Ro	Ac	P	N	Rc	Lc	$Vt\ /\ Va$	C	Re	Ls
[22]	12.7, 50.8, 76.2	114.5	NL	LEE	10.5, 17.5, 28	NL	NL	NL	NL	NL	NL
[23]	8	64 or 80	NL	5.5	5	NL	0.86	44349	40	25.5	2
[24]	NA	64	1.31	5.5	5	NV	NV	44353	40	25.5	2
[44]	31	75	0.2	5.5	5	NL	NL	44353	40	NL	NL
[32]	NV	NV	NV	NV	NV	NL	1.1	7.5/4-7.5	600	NL	1.61
[45]	NL	NL	NL	NL	9	NL	NL	NL	NL	NL	NL
[25]	8.45	NL	20.1	4.64	8	NL	NL	NL/3	390	125	8.4
[46]	NL	115	NL	NL	7	2.98	0.23	15/8	0.2	NI	NI

Continued Table 2.5 Specification of The Energy Source and Flat Spiral Coil

	Flat spiral coil						Energy Source				
[47]	NI	80	3.14	5.5	5	NI	NI	44349	40	28.5	2.86
[27]	8	64	NI	5.5	5	NI	NI	NI	NI	NI	NI
[48]	200	NI	NI	5(W)	8	NI	CL	25/CL	640	NI	NL
[49]	20	120	16	10	6	NL	1.03	0.9	8400	NL	NL
[50]	20(F)	72	4	NL	10/4ML	24.1	46.1	25/(s)	320	5	6
	140(R)	165	8	NL	5/4ML	20	85.7	25/(s)	320	5	6
	20(F)	72	4	NL	10/4ML	25.7	46.6	25/(s)	320	25	10.9
[52]	140(R)	165	8	NL	5/4ML	21	87.6	25/(s)	320	25	16

In this table: R_o stands for spiral coil outer Radius [mm]; Ri stands for spiral coil inner Radius [mm]; P stands for turns per unit length [mm]; Ac stands for cross-section area of the coil [mm²]; N stands for turns; L_c stands for coil self-inductance [μH]; R_c stands for coil electric resistance [mΩ]; Vt stands for extreme electric voltage [kV]; C stands for capacitance [[μF]; Re stands for resistance of electric circuit [mΩ]; CL stands for Dependent on the number of coil layers; V_a stands for discharge electric voltage [kV]; ML stands for multilayer; LEE stands for Method restricted to the side by side windings, Ls stands for inductance of electric circuit [[μH]; NL stands for not knowledgeable/presented; NV stands for not valid; (F) stands for Flat coil; (R) stands for Radial coil; (W) stands for Winding gap; (S) stands for Several electric potentials for flat and radial coils were used.

Chapter 3

Research Methodology

This chapter presents the methodology used in the present work. The methodology used in this research can be broadly divided into the two parts. The first part deals with the experimentation done in this research. The second part of methodology describes the numerical aspect of the research. **Figure 3.1** presents the methodology used in this research.
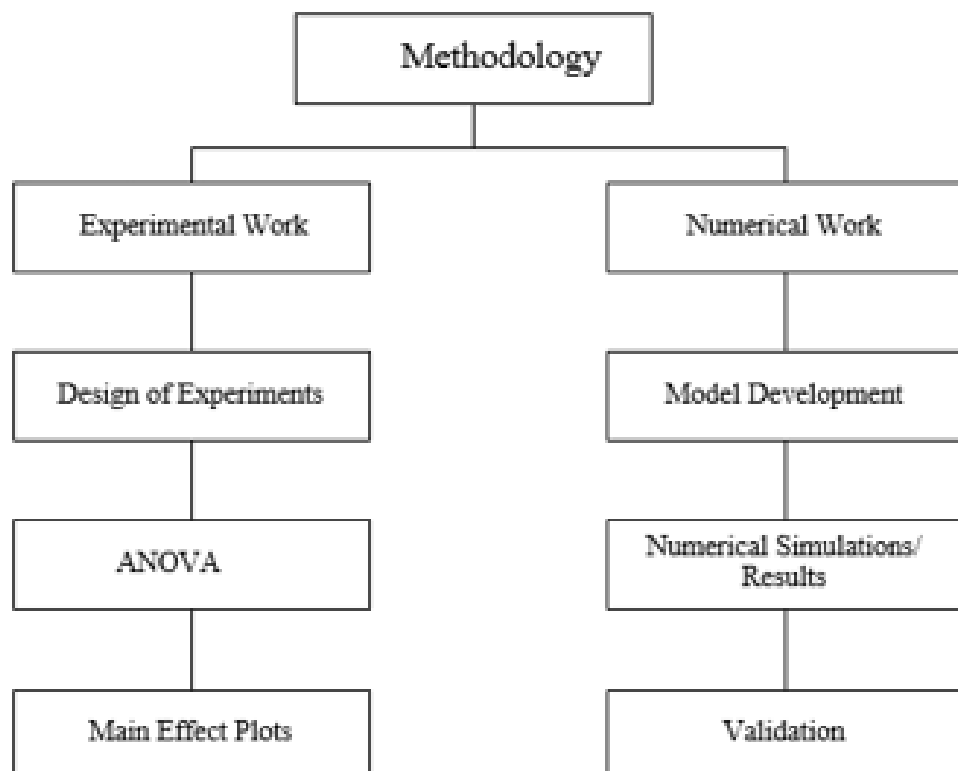
3.1   Experimental Work

The experimental work done in this research is presented in this section. In this regard, development of experimental setup, Design of Experiments (DOE), and statistical analysis of the data has been discussed in detail.

3.1.1   EMF Process Parameter

In EMF, the final deformed shape is dependent on number of process variables. Application of uniform magnetic pressure for forming of a specific shape is very critical. In this regard, actuator coil cross-sectional shape, the capacitance of capacitor bank, and discharge energy are the major factors for the uniform magnetic field [53]. The attributes/characteristics (height, thickness variation, microstructure) of the finally deformed work depends on the selected variables. The detailed discussion in Chapter 2 reveals that cross-sectional shape of coil, capacitance and energy level are the most important factors that affect the geometrical as well as metallurgical aspect of the finally deformed shape. Therefore, the effect of aforementioned factors on EMF process was investigated in the current research.

To study the effect of the coil cross-sectional shape on EMF, three different cross-sectional shapes of actuator coils having the same cross-sectional area were fabricated. To analyze the effect of energy on deformation, experiments were done on the three levels of the energy with the three different cross-sectional shape of actuator coil. In order to assess the effect of capacitance on EMF, the capacitor bank of 27 kJ maximum energy and capacitance ranges from 1500 μF to 5500 μF was used for experiments.

3.1.2   Development of Experimental Setup

3.1.2.1   Capacitor Bank

The schematic diagram of EMF process is shown in Figure 3.2, which shows the arrangement of an open die metal sheet for free bulging. The capacitor bank is attached in parallel with power supply and in series with the actuator coil.

Capacitor bank provides the output voltage that ranges from 100 V to 3000 V. Together these components forms a RLC circuit.
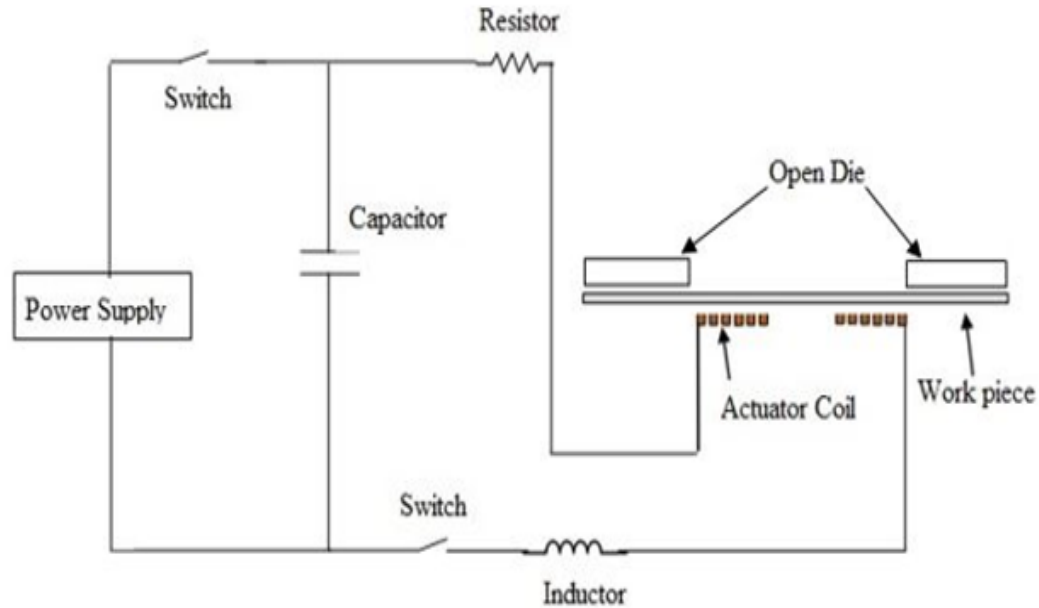
FIGURE 3.2: Schematic Diagram of EMF (adopted from [54])

A capacitor bank provides rapid energy discharge through the actuator coil for the forming process. Therefore, a capacitor bank is a significant component of the electromagnetic forming process. The capacitor bank used for current experimental work provides energy in the range of 1 kJ to 27 KJ as per the requirement. The operating parameters of the capacitor bank used in this research are given in **Table 3.1**: Parameters of the Capacitor bank.

TABLE 3.1: Parameters of the Capacitor bank

Parameters	Value
Input voltage (Va)	220-240 V AC
Capacitance (C)	$(500, 1000, 2500, 3500, 4000, 5500, 6000)\mu F$
Maximum Voltage (V)	3000 V DC
Maximum Energy	27kJ

3.1.2.2 Actuator Coil

In the EMF process, the actuator coil is the main component of the RLC circuit. Figure 3.3 shows the schematic of a standard rectangular cross-sectional actuator coil. In order to assess the effect of the cross-sectional shape of the actuator coil on EMF, three different cross-sectional shapes having the same cross-sectional area were fabricated for this research. The inner and outer diameter of the three actuator coils was kept constant. Different parameters of the developed coils are shown in **Table 3.2**.
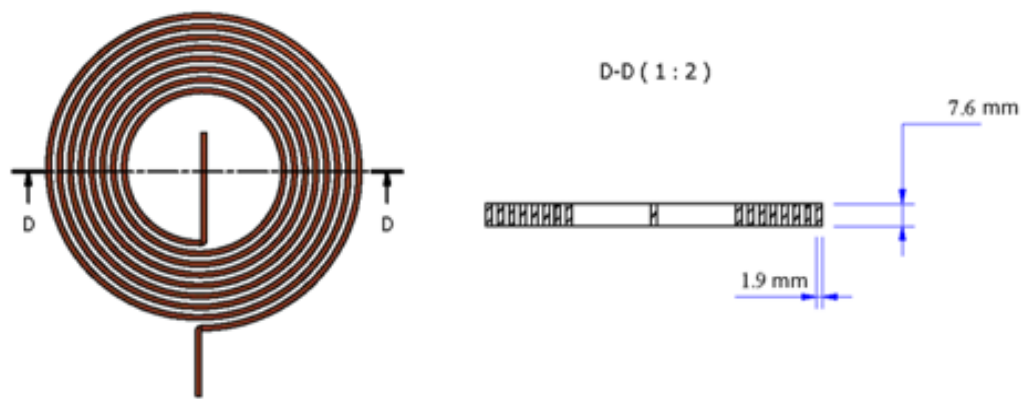
FIGURE 3.3: Schematic Diagram of Actuator Coil

TABLE 3.2: Description of Coil Parameter

Parameter	Circular Shape	Square	Rectangular
Cross-section dimension	d = 4.2 mm	X = 3.75 mm	w = 7.6, h = 1.9 mm
Inner Dia (Di)	52 mm	52 mm	52 mm
Outer Dia (Do)	130 mm	130 mm	130 mm
No of turns	6	6	6

For the fabrication of Square and Rectangular coil, the desired dimension was not available in the market. Therefore, both coils were made through CNC wire cut machine. Square Blank of 150 ×150 mm^2 with 5 mm and 9 mm thickness was

used for fabrication of square and rectangular cross-sectional shape of spiral coils respectively. A lathe machine was used to face the blanks for coils. Coils outer diameter was constant 130 mm and the inner diameter was 52 mm. A square coil is shown in Figure 3.5 before its fixation, and its electrical properties are given in Table 3.4.
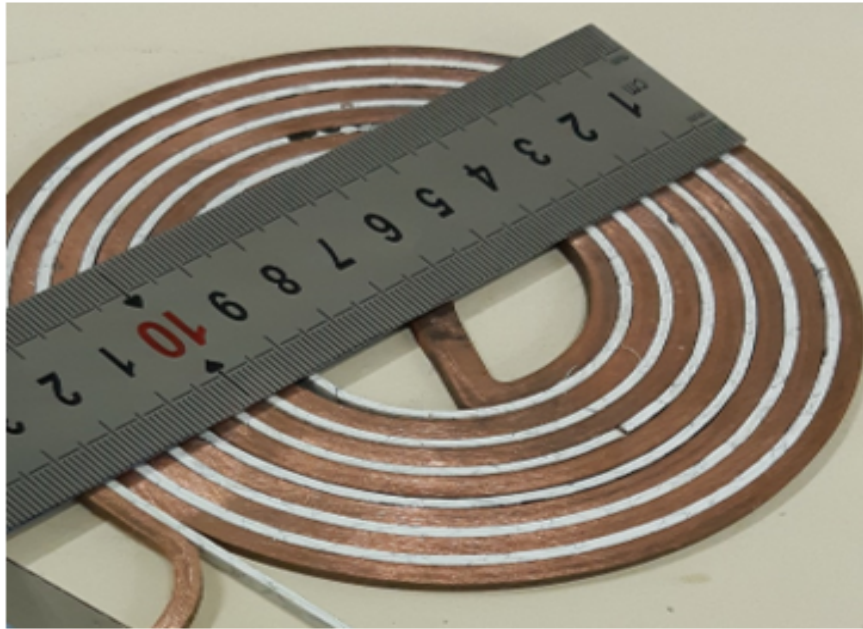
FIGURE 3.4: Coil before fixation

TABLE 3.3: Electrical Properties of the Actuator Coil

Electrical properties	Value
Material	Copper
Electrical Conductivity	5.998 e^7 S/m
Resistance of coil	5.2 mΩ
Inductance of coil	7.86 μH
Relative permeability	1
Relative permittivity	1
Reference Temperature	298 K

During the Electromagnetic forming process, a high current passes through the turns of coils and produces repulsive forces between turns. This repulsion is strong enough to damage the coil turns and can cause a short circuit of coil turns due

to high current. Therefore, the fixation of the coil is very important for the EMF process. Fiber wood, an insulator material was used to make a base for the coil. A counter-bore was done in a fiber wood sheet for two purposes. Firstly, it ensured that the actuator coil would not un-turn during the forming process. Secondly, the depth of the bore helped to maintain the gap between the coil and the workpiece. In order to provide insulation between the turns of a coil, a vinyl tile (a good dielectric material) spacer of 2 mm was used. Finally, epoxy resin was poured on the coil to provide strength to the coil (as shown in **Figure 3.6**).

FIGURE 3.5: Epoxy resin and coil fixation process in fiber wood

Figure 3.5. Epoxy resin and coil fixation process in fiber wood. Resistance (R_c) and inductance (L_1) of the copper coil (given in **Table 3.3**) were measured by RLC meter as shown in **Figure 3.7**. Pure copper (99.9%) was used for the fabrication of the coils.

FIGURE 3.6: Measurement of resistance (R_c) and inductance (L_1) of copper coil

3.1.2.3   Die for EMF

As the current research focused on the free-forming process, therefore an open-die was used. An open die has a circular opening in the center and it holds the workpiece from its edges. The circular opening in the center allows the free forming of workpiece sheets. **Figure 3.8** shows the schematic diagram of the open-die used in the current research.
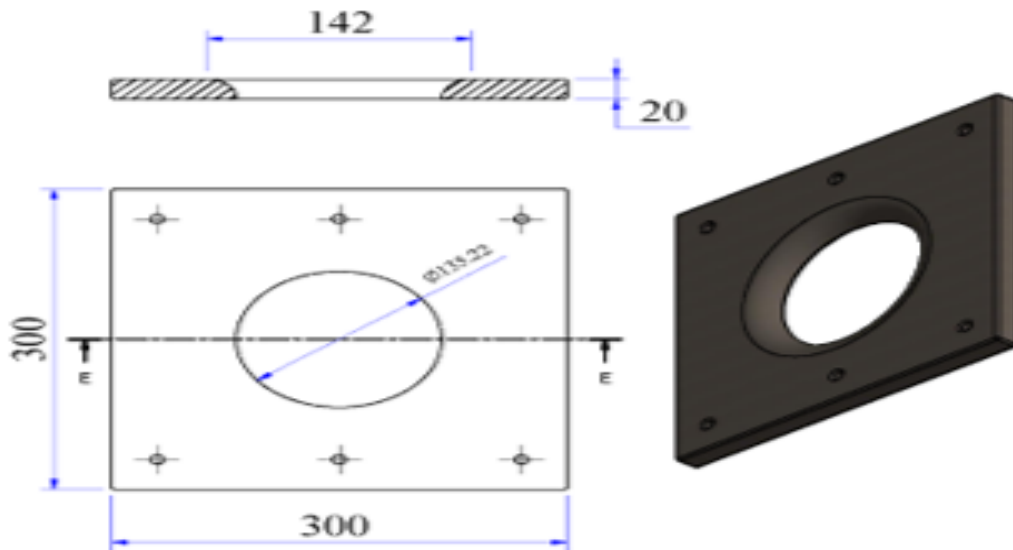
FIGURE 3.7: A detailed drawing and 3D model of the open-die

3.1.3   Complete Experimental Setup

In EMF, fixture consists of many parts, like as coil plate, die plate, backplate, and the number of bolts, etc. Fixture material must have non-magnetic properties for better result of EM sheet forming. Die can be made by non-magnetic material like PVC, fiber wood, Garolite, and steel. Machining cost of fiber wood was less than other materials, so that's why the fiber wood was selected for die making. Die and coil must have concentric for accurate EMF otherwise forming energy work will go wasted. In present work, die and coil plates were made concentric by using two dowel pins that helped in accurate alignment of the die and coil plate.

The complete experimental setup based on the circuit diagram (shown in **Figure 3.2**) was developed. In order to handle the high repulsive force, Chromium steel plates were mounted on both sides of the die. For holding, 6 bolt of M8 were used

for clamping in addition to a C-clamp. **Figure 3.8 (a) and (b)** shows the different components of the experimental setup and complete assembled experimental setup, respectively.
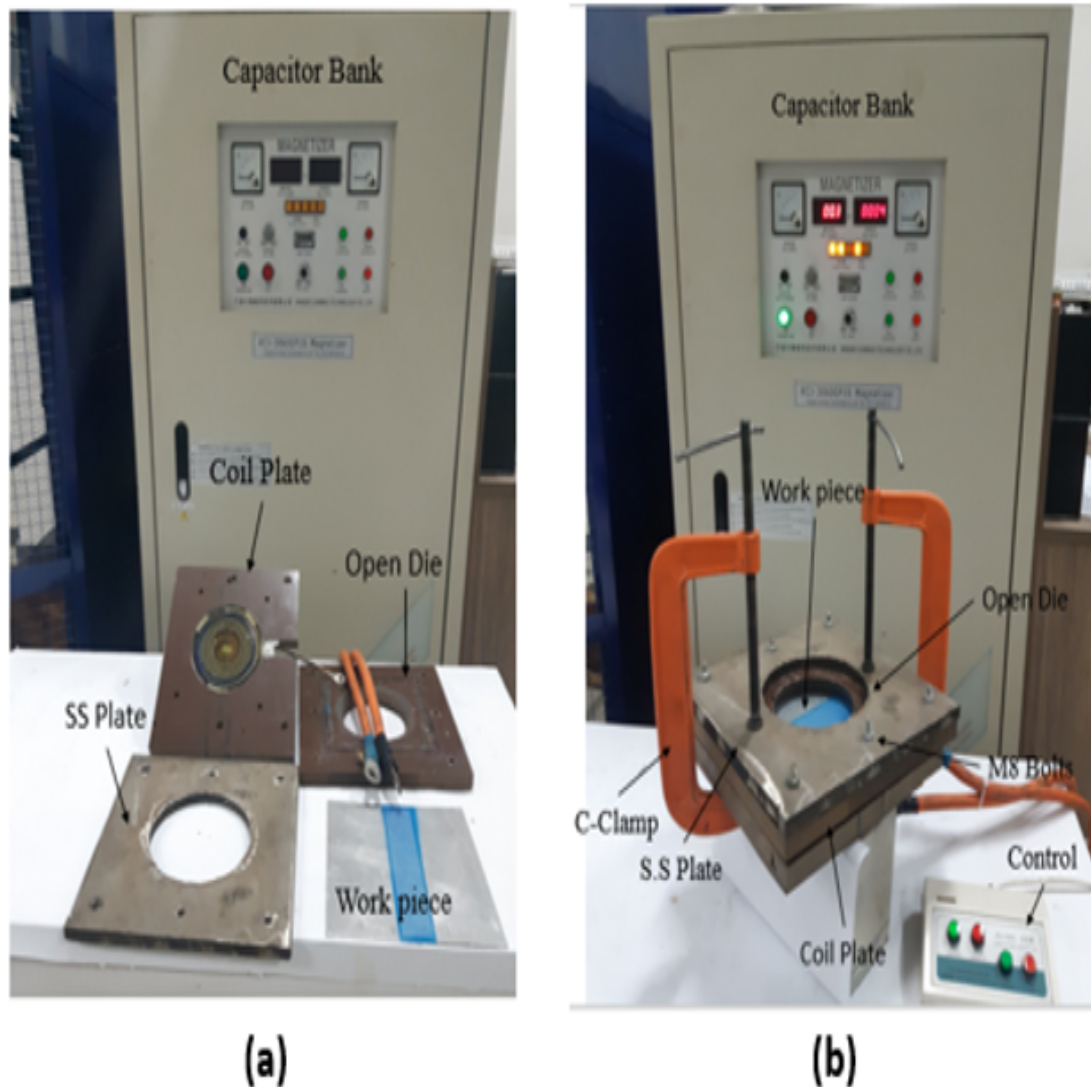
FIGURE 3.8: (a): Different components of setup, (b) complete assembled setup

3.1.3.1 Workpiece Material

Aluminum alloys are widely used for various engineering applications, e.g. in the automotive, aerospace industry, owing to their properties such as strength, lightweight, workability and corrosion resistance, etc. Therefore, the present research also used aluminum alloy Al 6061 as the workpiece material. The thickness of the aluminum alloy sheet was chosen as 1.25 mm in the current experimental work. Different properties of Al 6061 are given in **Table 3.4.**

TABLE 3.4: Properties of Aluminum Sheet [55]

Parameter	Value
Density (r)	2.7 g/cm3
Break Elongation	12-25%
Ratio of Poisson	0.33
Electrical resistivity Rw	3.9 e^{-4} W m
Ultimate tensile stress	310 MPa
Tensile Yield Strength	276 MPa
True stress	300-420 MPa
Young's modulus (E)	68.9 GPa

In the EMF process, an optical microscope was used for the investigation of the elongation of the surface of the deformed workpiece. A pattern was marked on the surface of the sheet by etching with laser marking. In the laser marking, the laser burnt the material surface and developed an oxide layer. Aluminum oxide color is the same as aluminum so that sheet was painted before deformation. Laser marking is shown in **Figure 3.9 (a) and (b)**.
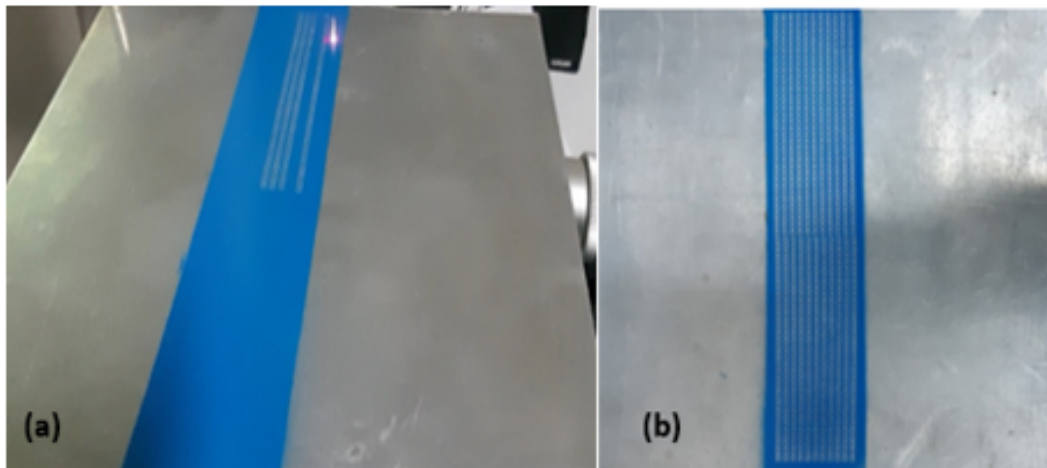
FIGURE 3.9: (a) During laser Marking (b) After Laser Marking

3.1.3.2 Experimental Design

The effect of input parameters on the height and thickness of deformed sheets were studied using the full factorial experimental design. Three levels each of coil

cross-sectional shape, energy, and capacitance were chosen as shown in **Table 3.5**. The complete experimental plan developed using full factorial DOE used in this research is shown in **Table 3.6**.

TABLE 3.5: Complete Experimental Plan Design of Experiments

Factors	Type	Levels	Values
Cross-section	Fixed	3	Circular (C), Rectangular (R), Square (S)
Energy level	Fixed	3	1, 2, 3
Capacitance	Fixed	3	2500, 4000, 5500

TABLE 3.6: Complete Experimental Plan Design of Experiments

S. No	Coil	Energy (kJ)	Capacitance mF	S. No	Coil	Energy (kJ)	Capacitance mF
A-1	S	1	2500	A-15	C	2	5500
A-2	S	1	4000	A-16	C	3	2500
A-3	S	1	5500	A-17	C	3	4000
A-4	S	2	2500	A-18	C	3	5500
A-5	S	2	4000	A-19	R	1	2500
A-6	S	2	5500	A-20	R	1	4000
A-7	S	3	2500	A-21	R	1	5500
A-8	S	3	4000	A-22	R	2	2500
A-9	S	3	5500	A-23	R	2	4000
A-10	C	1	2500	A-24	R	2	5500
A-11	C	1	4000	A-25	R	3	2500
A-12	C	1	5500	A-26	R	3	4000
A-13	C	2	2500	A-27	R	3	5500
A-14	C	2	4000				

3.2 Numerical Simulation

3.2.1 Working Principle

EMF equipment mainly includes a charging system, capacitor, discharge switch, coil system, and workpiece. Firstly, the capacitor is charged by the charging

system. Secondly, the stored energy is loaded into the coil system through the discharge switch to generate a pulse large current and a pulse strong magnetic field around the workpiece. Thirdly, the variational magnetic field produces induced eddy current in the workpiece. Finally, the electromagnetic force between the pulse current in the coil system and the induced eddy current in the workpiece deform the workpiece. **Figure 3.10** shows the analogous RLC circuit reflecting different phases of electromagnetic forming.
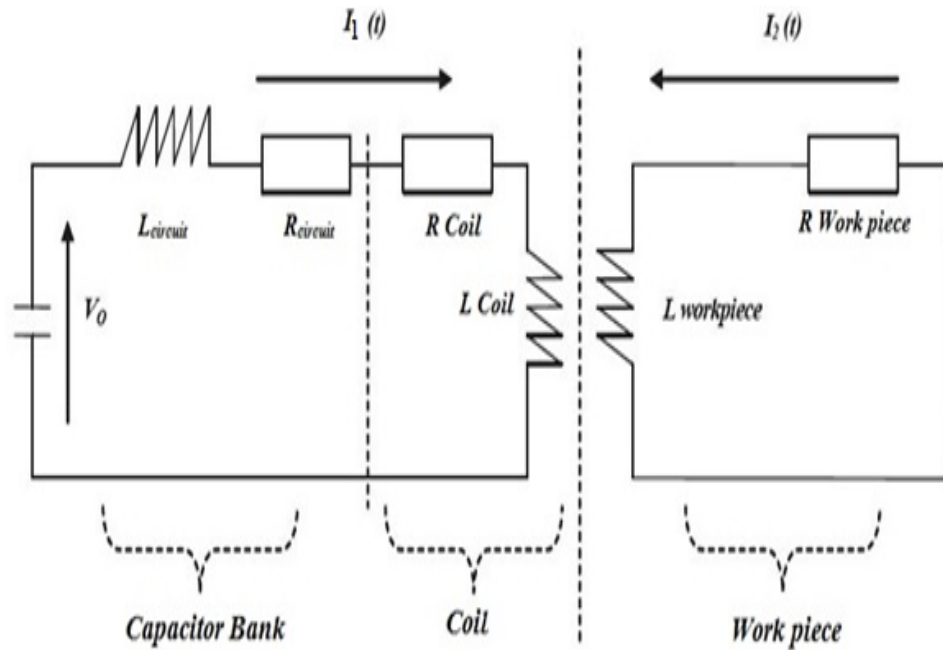

FIGURE 3.10: Analogous RLC Circuit Reflecting the Phase of Electromagnetic Formation

3.2.2 Physics Governing the EMF Process

Maxwell's equations [56] given below are used to solve magnetic fields.

$$\Delta.\bar{j} = 0 \tag{3.1}$$

$$\Delta.\overline{B} = 0 \tag{3.2}$$

$$\overline{\beta} = \mu\overline{H} \tag{3.3}$$

$$\Delta \times \overline{H} = \overline{J} \tag{3.4}$$

$$\Delta \times \overline{E} = \frac{1}{dt} \tag{3.5}$$

Where μ is Permeability (H/m), B is the Magnetic Field Density T (Wb/m^2), E is the Electric Field (V/m), J is Current Density (A/m2) and H is the Magnetic Field Intensity (A/m).

$$\overline{j} = \sigma \overline{E} \tag{3.6}$$

Where σ (ohm/m) is the electrical conductivity of the workpiece. Lorentz force depends on the magnetic flux density (T) **B** and current density **J** (A/m^2), can be calculated by **equation 3.7**.

$$\overline{F} = \overline{J} \times \overline{B} \tag{3.7}$$

$$\overline{j} = \frac{\partial H}{\partial Z} \tag{3.8}$$

According to Bauer [57], the forces acting on the metal sheet can be determined by **Equation 3.9**:

$$Fz = -\mu H \frac{\partial H}{\partial Z} = -\frac{1}{2}\mu \frac{\partial (H)^2}{\partial Z} \tag{3.9}$$

3.2.3 Modeling of EMF

A spiral coil system can be equivalent to a plurality of radially distributed closed rings. And then, the coil system, the workpiece, and the electromagnetic field source are all axial symmetrical, hence it can be simplified as a two-dimensional axisymmetric model. The Maxwell equation is used for numerical simulation. In this study, Simulations were carried out in COMSOL using AC/DC module and Structural-Mechanics module. The flow chart of numerical simulation in COMSOL is given below in **Figure 3.11**.
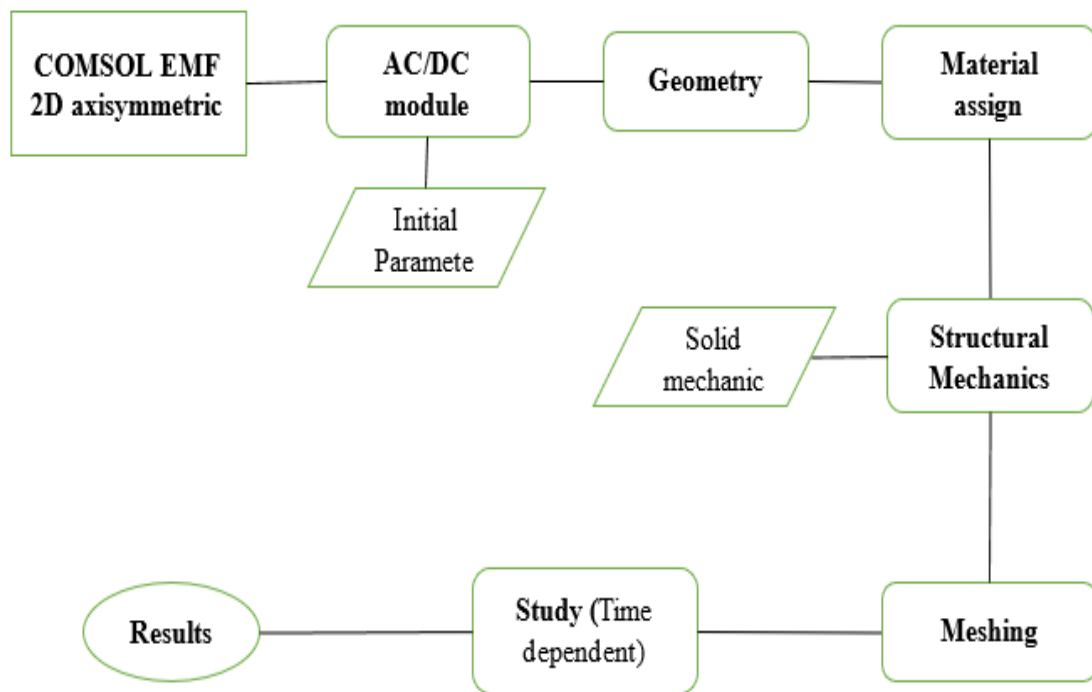
FIGURE 3.11: Flow chart of COMSOL EMF Sheet Forming Process

3.2.3.1 Assumption of EMF Model

1. The discharge current of the capacitor bank is uniformly distributed in the cross-section of the coil.

2. The displacement of current is neglected.

3. Inductance is constant during the discharging of the capacitor bank through the coil.

4. The permeability and conductance of materials are constant and isotropic.

3.2.3.2 Geometry and Meshing

In this research, the geometry of the EF model was used to initiate the free bulging process of the EM sheet which is shown in **Figure 3.12**. Because of the axial symmetry of both the sheet and the coil one half of the mechanism of the formation was considered in the two-dimensional FE model. All entire geometry mesh for the propagation of magnetic field.
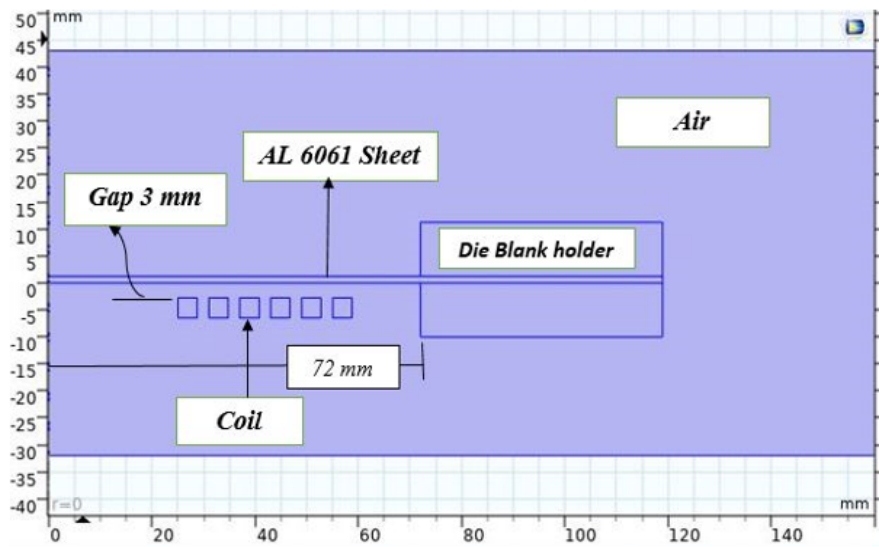
FIGURE 3.12: Geometry for Numerical Modelling

The meshed type of free triangular was adopted is shown in **Figure 3.13 and 3.14**. The total number of elements is 7122, and the total area meshed is 15490 mm^2.
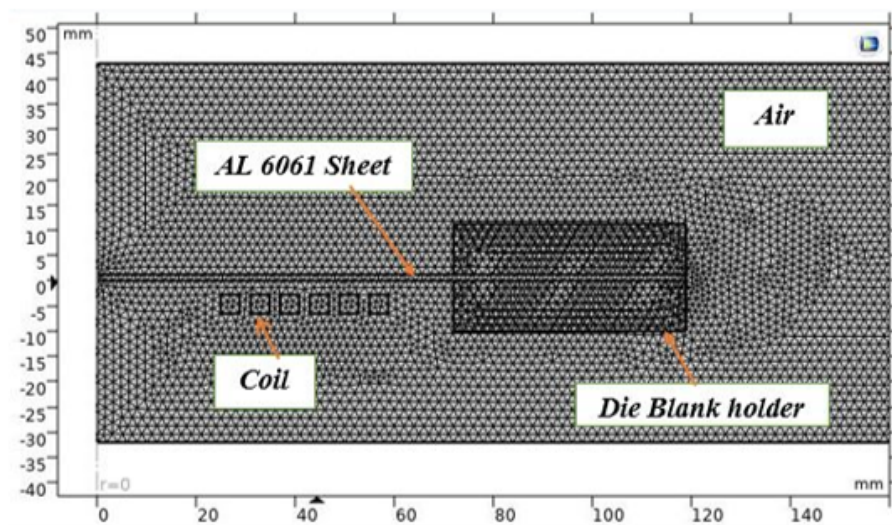
FIGURE 3.13: Meshing of Entire Geometry

3.2.4 Boundary Conditions

In electromagnetic sheet forming 2D axisymmetry model used for numerical simulation. COMSOL multiphysics used Neuman boundary as the default for axisymmetry.
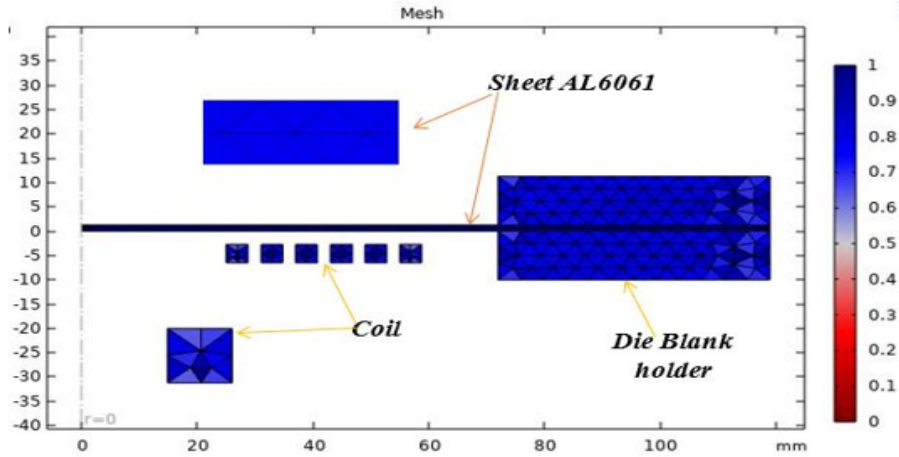
FIGURE 3.14: Meshing of Entire Geometry

3.2.5 Material Model

The constitutive behavior of the workpiece material is described in **Fig. 3.15**. The quasi-static stress for numerical model is used from **Figure 3.15**. Cowper–Symonds model is adopted for solid mechanics model

$$\sigma = \sigma_y \left[1 + \left(\frac{\varepsilon}{P} \right)^m \right] \tag{3.10}$$

Where dynamic flow stress is σ, quasi-static flow stress is σ_y, ε is the strain rate, whereas P=6500 1/s and m =0.25 [58].
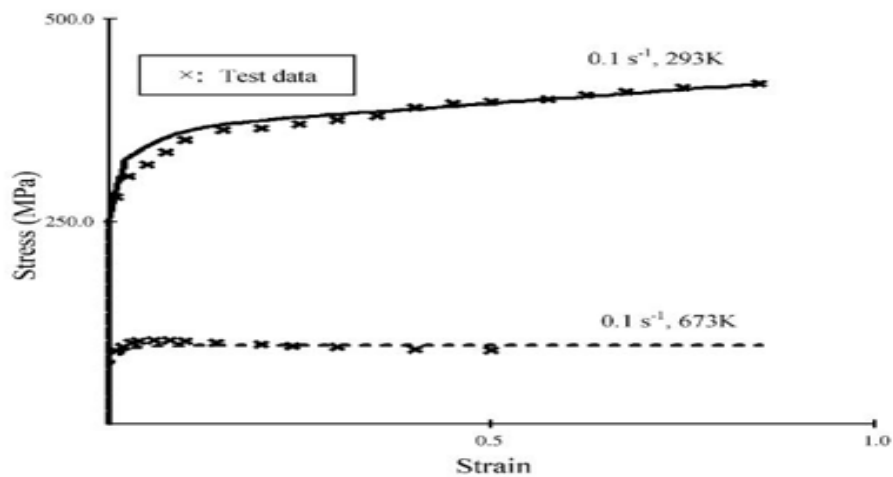
FIGURE 3.15: Constants of Materials based on Test Data at Temperature 293K and 673 K of AL 6061-T6 [59]

3.2.6   Process Parameters

Simulated parameters of EMF are given below in **Table 3.7**.

TABLE 3.7: Initial process parameters for Numerical Model

S. No	Cross-section	Energy	C_o	U_o	R_e	L_e	σ y	Cowper Symonds constant [58]		
		kJ	(μF)	(V)	W	μH	(MPa)	P(1/s)	m	
										(1/s)
1	S	1	2500	895	0.0052	7.86	350	6500	0.25	0.001
2	S	1	4000	707	0.0052	7.86	350	6500	0.25	0.001
3	S	1	5500	603	0.0052	7.86	350	6500	0.25	0.001
4	S	2	2500	1265	0.0052	7.86	350	6500	0.25	0.001
5	S	2	4000	1000	0.0052	7.86	350	6500	0.25	0.001
6	S	2	5500	853	0.0052	7.86	350	6500	0.25	0.001
7	S	3	2500	1550	0.0052	7.86	350	6500	0.25	0.001
8	S	3	4000	1225	0.0052	7.86	350	6500	0.25	0.001
9	S	3	5500	1045	0.0052	7.86	350	6500	0.25	0.001
10	C	1	2500	895	0.0052	7.86	350	6500	0.25	0.001
11	C	1	4000	707	0.0052	7.86	350	6500	0.25	0.001
12	C	1	5500	603	0.0052	7.86	350	6500	0.25	0.001
13	C	2	2500	1265	0.0052	7.86	350	6500	0.25	0.001
14	C	2	4000	1000	0.0052	7.86	350	6500	0.25	0.001

Continued Table: 3.7 Initial process parameters for Numerical Model

S. No	Cross-section	Energy	C_o	U_o	R_e	L_e	σ y	Cowper Symonds constant [58]		
15	C	2	5500	853	0.0052	7.86	350	6500	0.25	0.001
16	C	3	2500	1550	0.0052	7.86	350	6500	0.25	0.001
17	C	3	4000	1225	0.0052	7.86	350	6500	0.25	0.001
18	C	3	5500	1045	0.0052	7.86	350	6500	0.25	0.001
19	R	1	2500	895	0.0052	7.86	350	6500	0.25	0.001
20	R	1	4000	707	0.0052	7.86	350	6500	0.25	0.001
21	R	1	5500	603	0.0052	7.86	350	6500	0.25	0.001
22	R	2	2500	1265	0.0052	7.86	350	6500	0.25	0.001
23	R	2	4000	1000	0.0052	7.86	350	6500	0.25	0.001
24	R	2	5500	853	0.0052	7.86	350	6500	0.25	0.001
25	R	3	2500	1550	0.0052	7.86	350	6500	0.25	0.001
26	R	3	4000	1225	0.0052	7.86	350	6500	0.25	0.001
27	R	3	5500	1045	0.0052	7.86	350	6500	0.25	0.001

Chapter 4

Data Analysis and Discussion

This chapter discusses the experimental results of the EM sheet forming with respect to the input variables. The obtained results have been analyzed with ANOVA and main effect plots. The responses obtained from the experimental plan are presented in **Table 4.1**.

It can be observed from the **Table 4.1** that axial Dome height increases by increasing the energy level and decreases by increasing the capacitance of the capacitor bank.

The Maximum Dome height is observed in the square coil and minimum Dome height is observed in the rectangular coil. Statistical analysis is done, to examine the effects of the variable on the responses, and also optimize the factors for EM sheet forming.

4.1   Dome Height and Deformation Morphology

This part of the study aims to evaluate the effect of process variables on Dome height and profile shape. The quantitative results of experimental Dome height are given in **Table 4.1**.

The pictorial presentation of the deformed workpiece is shown in **Figure 4.1** (workpiece deformed at 3 kJ energy, 2500 μF capacitance by using the square coil). The maximum Dome height was measured in the A-7 experiment.

TABLE 4.1: Experimental Results

Input Parameters of EMF				Responses of EMF				
S. No	Coil cross-section shape	Capacitance (μF)	Energy Level (kJ)	Dome height (mm)	Thickness Distribution Max (mm)	Min (mm)	Std. Dev.	Exp. peak current (kA)
A-1	S	2500	1	8.95	1.27	1.2	0.020256	14.1
A-2	S	4000	1	7.8	1.26	1.2	0.01745	13.7
A-3	S	5500	1	6.85	1.26	1.23	0.010588	13.2
A-4	S	2500	2	17.27	1.29	1.19	0.029797	19.8
A-5	S	4000	2	14.28	1.28	1.2	0.024964	19.2
A-6	S	5500	2	11.55	1.27	1.21	0.017813	18.8
A-7	S	2500	3	22.39	1.28	1.18	0.027272	23.9
A-8	S	4000	3	20.44	1.3	1.19	0.032983	23
A-9	S	5500	3	18.15	1.29	1.19	0.027335	22.8
A-10	C	2500	1	8.3	1.26	1.2	0.016783	13.6
A-11	C	4000	1	7.52	1.26	1.2	0.016344	13.2
A-12	C	5500	1	6.41	1.26	1.24	0.005703	12.9
A-13	C	2500	2	14.23	1.28	1.2	0.024991	18.8
A-14	C	4000	2	10.58	1.27	1.2	0.020432	18.2
A-15	C	5500	2	9.59	1.27	1.2	0.019133	18.1
A-16	C	2500	3	17.862	1.28	1.19	0.022718	22.9

Continued Table: 4.1 Experimental Results

| Input Parameters of EMF				Responses of EMF				
S. No	Coil cross-section shape	Capacitance (μF)	Energy Level (kJ)	Dome height (mm)	Thickness Distribution			Exp. peak current (kA)
					Max (mm)	Min (mm)	Std. Dev.	
A-17	C	4000	3	17.24	1.28	1.19	0.025102	21.9
A-18	C	5500	3	14.58	1.28	1.2	0.02501	21.8
A-19	R	2500	1	5.27	1.26	1.21	0.013074	12.3
A-20	R	4000	1	4.92	1.26	1.22	0.011853	11.8
A-21	R	5500	1	4.37	1.26	1.23	0.009113	11.5
A-22	R	2500	2	13.66	1.27	1.2	0.018073	16.8
A-23	R	4000	2	11.35	1.27	1.2	0.019367	16.6
A-24	R	5500	2	9.88	1.27	1.2	0.020356	16.2
A-25	R	2500	3	17.04	1.28	1.19	0.025842	20.4
A-26	R	4000	3	13.95	1.28	1.2	0.024884	19.7
A-27	R	5500	3	11.29	1.27	1.2	0.020216	19.6
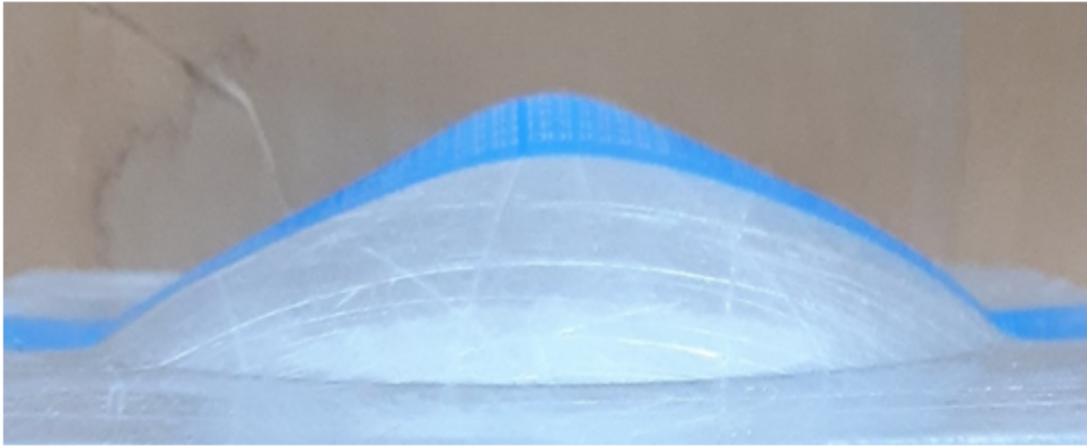
FIGURE 4.1: The deformed workpiece (A-7)

Deformations observed in workpiece for the complete experimental plan is presented in **Figure 4.2 (a, b, c)**. The maximum Dome height was observed in experiment No A-7 from **Table 4.1**, and minimum Dome height was observed experiment A-21. The profile of the deformed workpiece was mapped by using the CMM probe.
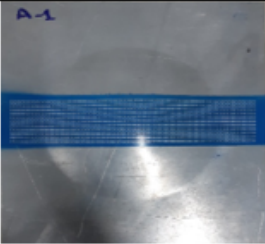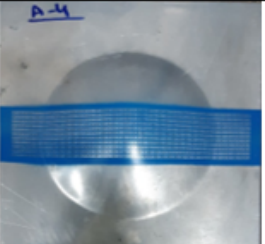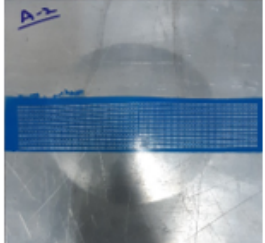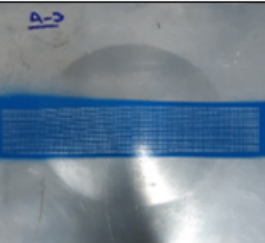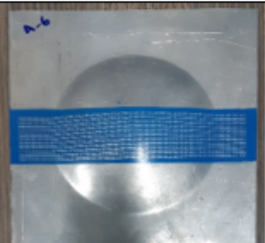
Exp. No	Actual Deformation	Exp. No	Actual Deformation
A-01		A-04	
A-02		A-05	
A-03		A-06	

FIGURE 4.2: (a) Deformed workpiece for the complete experimental plan
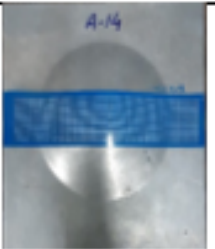
Exp. No	Actual Deformation	Exp. No	Actual Deformation
A-07		A-13	
A-08		A-14	
A-09		A-16	
A-10		A-17	
A-11		A-18	
A-12		A-19	

Figure 4.2 (b) Deformed workpiece for the complete experimental plan
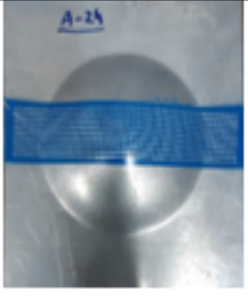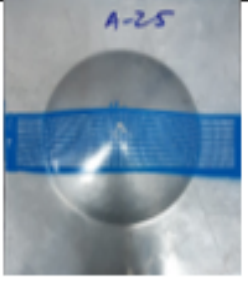
Exp. No	Actual Deformation	Exp. No	Actual Deformation
A-20		A-24	
A-21		A-25	
A-22		A-26	
A-23		A-27	

Figure 4.2 (c) Deformed workpiece for the complete experimental plan

Figure 4.2 presents the effect of coil cross-sectional shape on the Dome height of workpiece sheet. Energy level and capacitance were fixed at 3 kJ and 2500μF, respectively and only cross-sectional shape of the coil was varied. It can be seen from the **Figure 4.3** that square cross sectional shape produces maximum Dome height. This is because the magnetic flux density is highest in square shaped coils [60]. High magnetic flux density results in high Lorentz force that is responsible for producing deformation in the workpiece.
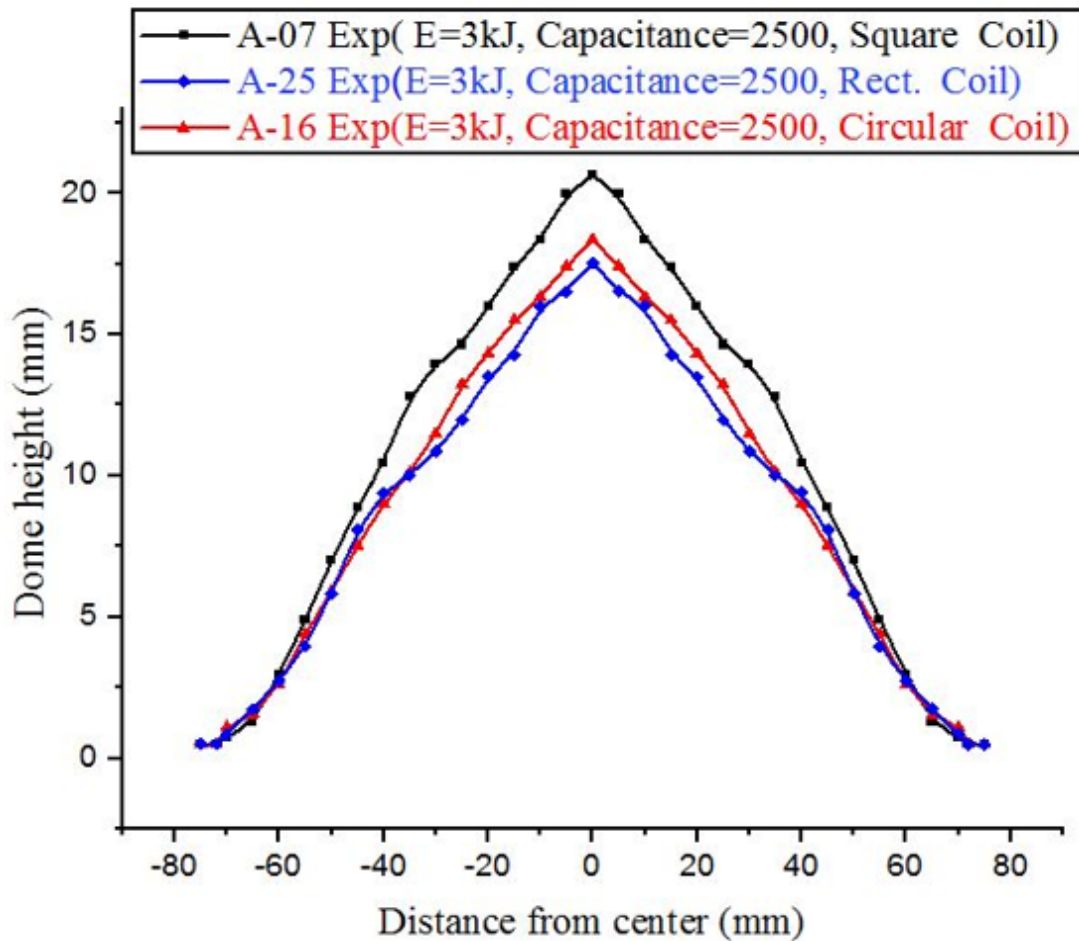
FIGURE 4.3: Comparison of the experimental result

4.2 Effect of Process Parameters on Dome Height

In order to assess the effect of process parameters (energy, capacitance, cross-sectional shape) on Dome height in EMF process, main effect plot was developed. **Figure 4.3** shows the main effect plot for Dome height. It can be seen for figure that Dome height is maximum at square cross-sectional shape in combination with highest energy level (3 kJ) and lowest capacitance level (2500 μF).

Highest energy level results in high magnetic field, high current peak and consequently high Lorentz force. This in turn increases the Dome height and results in high deformation. When capacitance decreases, current increases [18] which will also result in high magnetic field and high Lorentz force.
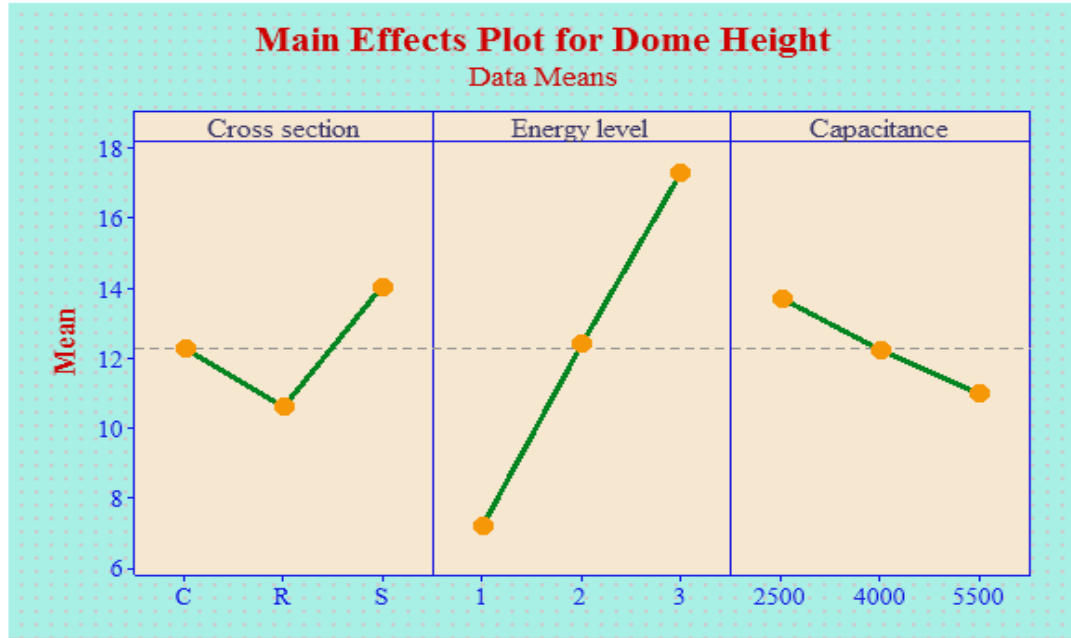
FIGURE 4.4: Main effect plot for maximum Dome heights.

The effect of process parameters on EMF process has also been investigated with Analysis of Variance (ANOVA). The results of ANOVA are presented in **Table 4.2**. It can be seen from the results that all process parameters (cross-sectional shape, energy level and capacitance) are statistically significant for Dome height (having P-value less than 0.05). In terms of percentage contribution, energy level has the highest influence (79%) and capacitance has least effect on Dome height. The importance of energy for Dome height (also discussed in previous section) is critical since higher energy warrants higher magnetic flux density and thus higher Lorentz forces that in turn result in enhanced deformation and greater axial deformation.

TABLE 4.2: Analysis of Variance of Dome height

Source	DF	Seq SS	Contribution	Adj SS	Adj MS	F-Value	P-Value
Cross-section	2	53.73	9.23%	53.73	26.866	15.56	0
Energy level	2	460.1	79.04%	460.1	230.049	133.23	0
Capacitance	2	33.74	5.80%	33.74	16.868	9.77	0.001
Error	20	34.53	5.93%	34.53	1.727		
Total	26	582.1	100.00%				

4.3   Thickness Variation of Deformed Workpiece

The deformed work piece was divided into three regions according to thickness distribution along its radial direction. Region A is top of the dome starting from zero to 15 mm from the center of the sheet. Region B is from 15 mm away from the center of the sheet up to 55 mm away from the center of sheet and remaining region is denoted by C showed in **Figure 4.5**.
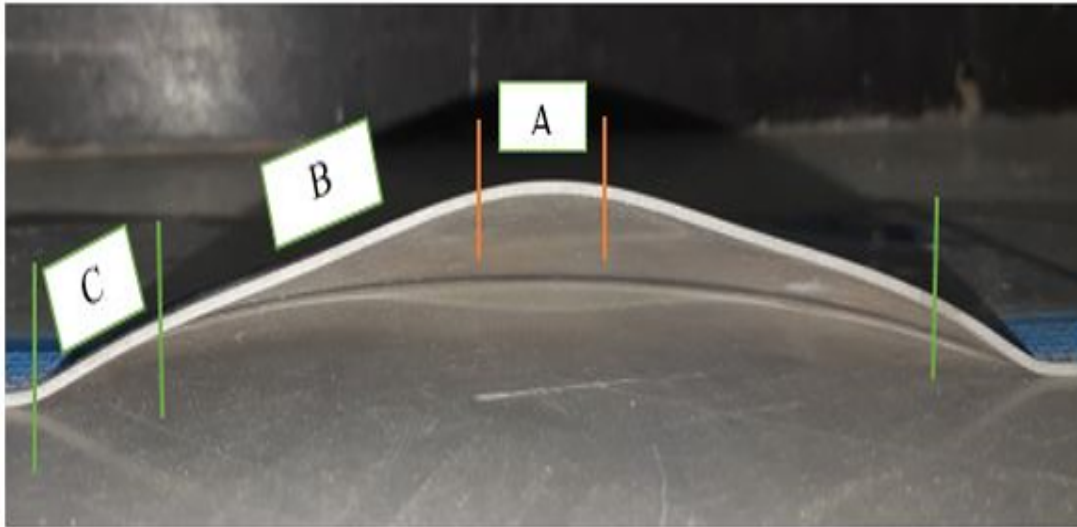
FIGURE 4.5: Cut off deformed work piece

The thickness of sheet was measured in these regions with the help of a Vernier caliper. The maximum thickness was observed in region A and minimum thickness in region B. These variations in thickness are also in alignment with the published literature. This variation in thickness is presented in graphical form in **Figure 4.5** where the thickness variation of best sample (Exp. # A-7) and worst sample (Exp. # A-21) has been compared. A detailed insight into the forming process of A-07 work piece reveals that workpiece got completely deformed in 430 μs, but the maximum Lorentz force was observed at 190 μs having a magnitude of 12.9 $\times$ 10^8 N/m^3. Similarly, maximum magnetic field was observed at 222 μs having a magnitude of 3.64 T. This suggests that work piece deformed due to inertial effect from 230 μs to 430 μs. The work piece gained high velocity in the start of EMF process, that caused work piece deformation due to inertial effect [61][62]. The material flowed from region B to region A due to high velocity and inertial

effect. The maximum thickness measured in region A was 1.28 mm and minimum thickness was measured as 1.19 mm at the point of 15 mm away from the sheet center (in region B). However, the thickness increased in radial direction away from B toward region C. As region C was near the die clamp and it also experienced the least magnetic field, thickness variation was not observed in that region. The general trend was observed in all the samples and it corroborates the findings of earlier studies [61][62].
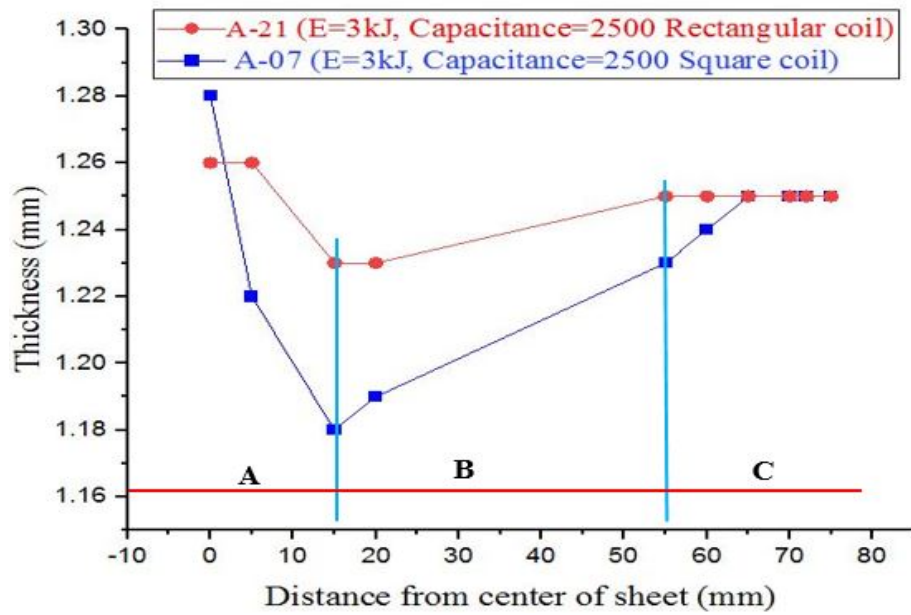
FIGURE 4.6: Thickness variation in A-7 and A-21
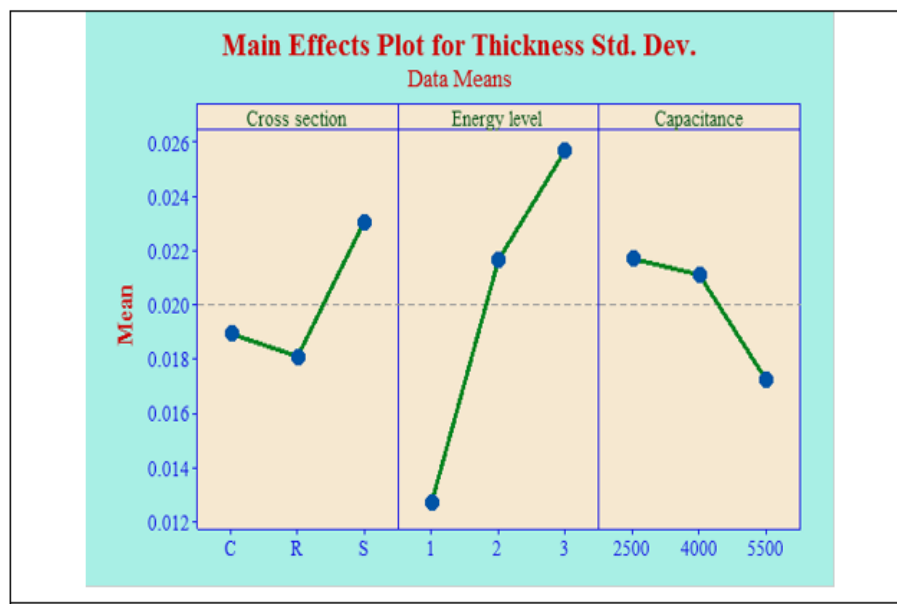
FIGURE 4.7: Main effect plot for thickness reduction standard deviation

Main effect plot of thickness variation was also plotted as shown in **Figure 4.7**. It can be that rectangular shaped coil gives the least thickness variation. Furthermore, energy level should be kept at lowest level and capacitance at highest possible level to obtain minimum variation in the thickness of the deformed workpiece.

ANOVA was also performed to assess the effect of process parameters on thickness variation in EMF process **(Table 4.3)**. ANOVA results reveal that energy level significantly influences thickness variation. Cross sectional shape and capacitance have almost same effect on thickness variation in EMF process.

TABLE 4.3: Analysis of Variance for thickness variation

Source	DF	Seq SS	Contribution	Adj SS	Adj MS	F-Value	P-Value
Cross-section	2	0.000127	10.95%	0.000127	0.000064	9.61	0.001
Energy level	2	0.000798	68.64%	0.000798	0.000399	60.27	0
Capacitance	2	0.000105	9.02%	0.000105	0.000052	7.92	0.003
Error	20	0.000132	11.39%	0.000132	0.000007		
Total	26	0.001163	100.00%				

4.4 Consolidated Results

Main effect plots developed in **Figure 4.4** and **Figure 4.7** revealed that the optimum setting of process parameters for Dome height and thickness variation are different (as shown in **Table 4.4**). These results build the case of case of multi-objective optimization. This avenue can be further explored and is recommended as future work.

TABLE 4.4: Consolidated Main effect plot results

Responses		Avg. Value	Energy (kJ)	Cross-Sectional Shape	Capacitance (μF)
			EMF Parameters and their levels		
Dome height	Best	22.39	3	S	2500
	Worst	4.37	1	R	5500
Thickness Variation	Best	0.0057	1	R	5500
	Worst	0.033	3	S	2500

4.5   Optical Microscope Analysis

The elongation in the deformed workpiece is evaluated by using the optical microscope. The microscope picture of the original sample is shown in **Figure 4.8**, and the deformed sample result is shown in **Figure 4.9**. The original sample dimension is mapped by an optical microscope. The laser box size is measured as 1367 μm $\times$ 1405 μm. After deformation of the workpiece, the dimension of the laser box are increased 6.67% in the radial direction and 7.3% in the transverse direction. This elongation is the evidence of material flow during the deformation of the workpiece. This suggests that material flow in the EMF increases the formability of the work piece due to high velocity and inertial effect [63].

The original and deformed workpiece were also analyzed under Scanning Electron Microscope (SEM). In this regard, unreformed workpiece, best (A-7) and worst (A-21) samples for axial deformation were analyzed (results shown in **Table 4.6**). SEM micrographs reveal that cracks are neither developed nor propagated in EMF process of Al 6061-T6 sheets. This is in contrary with quasi-static forming of aluminum alloys that results in crack development [55]. The ability of EMF process to avoid cracks in workpiece material highlights another benefits of this process.
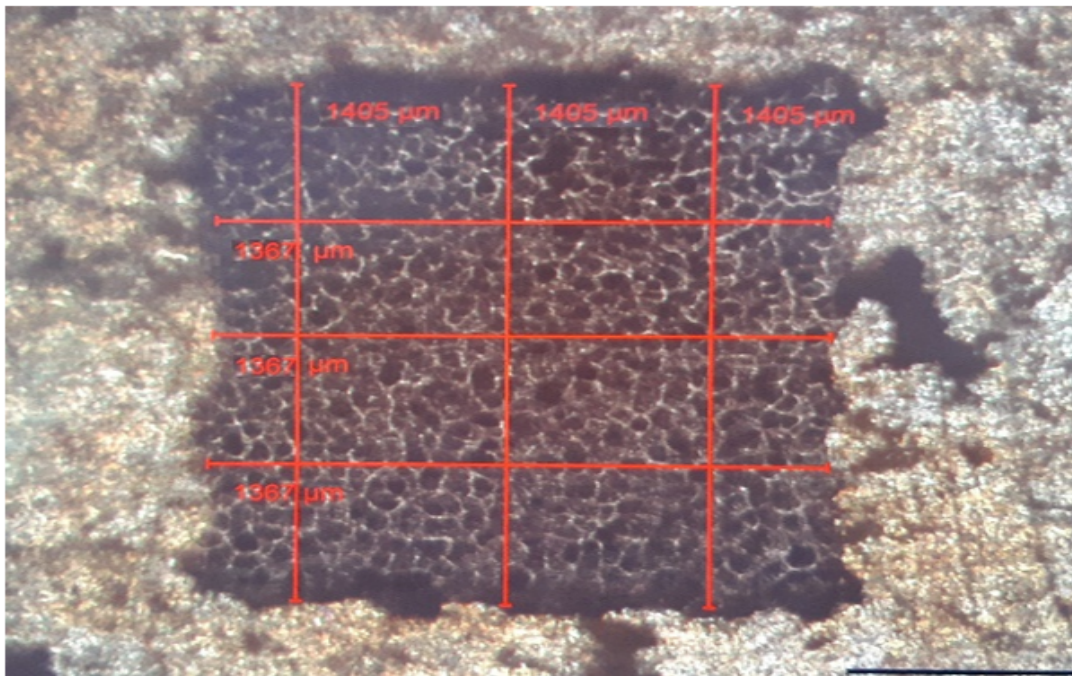
FIGURE 4.8: Al 6061 Before Deformation
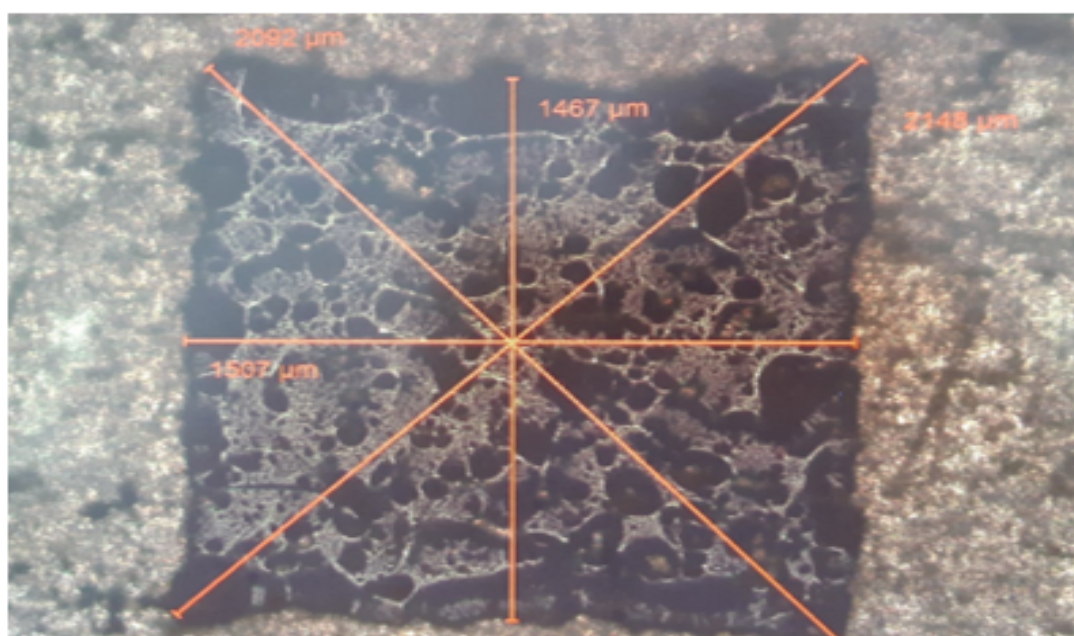
FIGURE 4.9: Al 6061 After Deformation
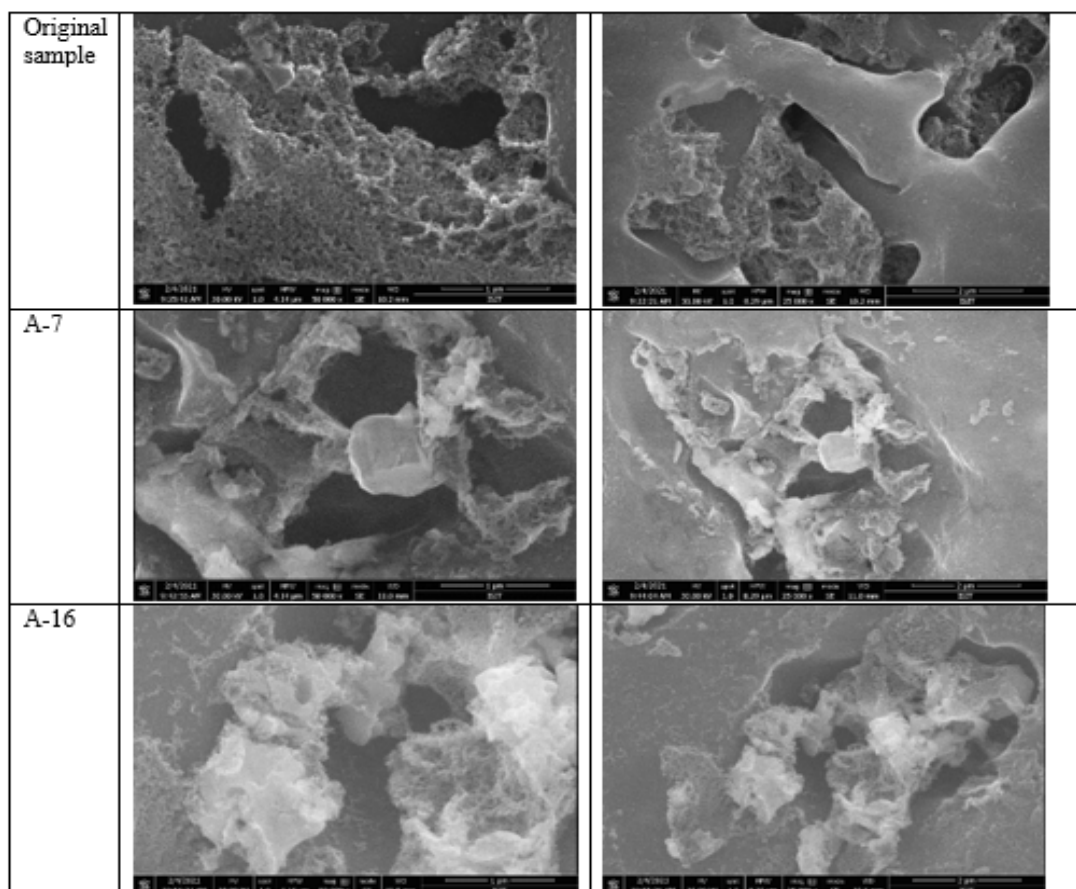
FIGURE 4.10: SEM Results

Chapter 5

Discussion and Conclusion

This chapter describes the numerical results of the electromagnetic model, solid mechanics model, and its comparison with the experimental result. The output of the electromagnetic model is used as an input in the solid mechanic's model. The numerical results were validated with outcomes from experimental results.

5.1 Numerical Results of the Electromagnetic Model
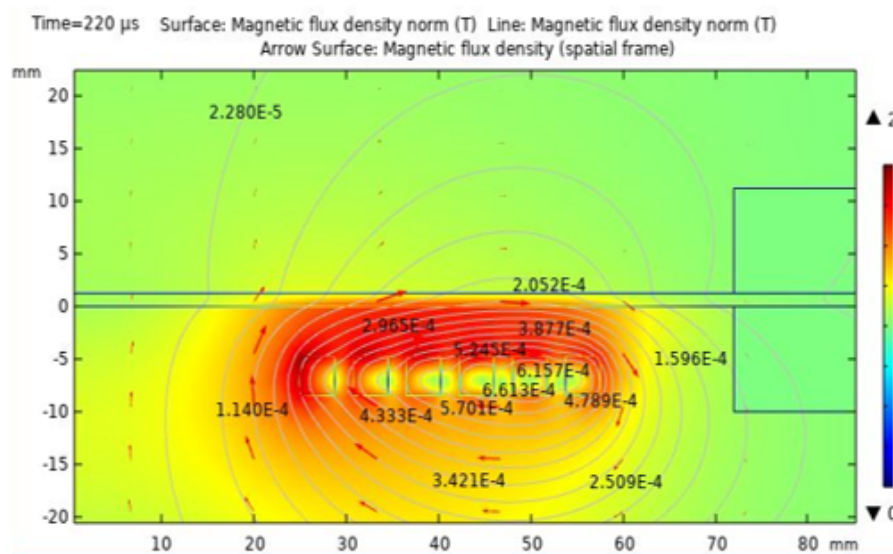
FIGURE 5.1: Magnetic flux behavior at the level of 1kJ energy, 2500 μF capacitance with square cross-section shape of the spiral coil.

The electromagnetic model consists of the magnetic flux density, Lorentz force, and current flow through the coil. The main component of the workpiece motion in electromagnetic sheet forming process is the axial direction which is determined by the axial velocity and the radial magnetic flux density.

T is the unit of magnetic flux density. The vertical axis shows the bottom and top of the sheet region where magnetic flux is produced. The horizontal axis shows the distance from the center of the sheet.

5.1.1   Magnetic Flux Density

The distribution of magnetic flux density with maximum of discharge current time is shown in **Fig. 5.1**. As time increases, the closed magnetic flux moves down from the center of coil to that of workpiece. At the same time, the induced magnetic field produced by the eddy current of workpiece gets stronger and the magnetic force acting on the workpiece increased. Most of the magnetic flux accumulates on the lower surface of workpiece.

The direction of magnetic flux distributing on the lower surface of workpiece is mainly parallel to the radial direction of workpiece, and the direction of magnetic flux distributing on the upper surface is mainly parallel to the axial direction of workpiece. Therefore, the axial component of magnetic force acting on the lower surface of workpiece is much larger than that acting on the upper surface. The difference between them is the electromotive force responsible of axial workpiece velocity.

The distribution of the magnetic flux density at peak discharge current time with the different coil cross-sections and different energy levels are given in **Table No 5.1**.

S is the square cross-section of the coil, Cir is the circular cross-section shape of the coil, R is the rectangular cross-section shape of the coil. Magnetic flux density behavior varied with change of capacitance, energy level, and coil cross-section. It is noticed that the magnetic flux density decreased with the increased level of capacitance at the fixed energy level.

TABLE 5.1: Magnetic flux density with respect to time

S. No	Coil cross-section shape	Capacitance (μF)	Energy Level (kJ)	Magnetic Flux density (T)	Time (μs)
A-1	S	2500	1	1.96	225
A-2	S	4000	1	1.92	270
A-3	S	5500	1	1.89	340
A-4	S	2500	2	2.86	220
A-5	S	4000	2	2.79	270
A-6	S	5500	2	2.71	330
A-7	S	2500	3	3.64	222
A-8	S	4000	3	3.59	283
A-9	S	5500	3	3.45	351
A-10	C	2500	1	1.84	206
A-11	C	4000	1	1.8	276
A-12	C	5500	1	1.74	354
A-13	C	2500	2	2.72	225
A-14	C	4000	2	2.68	276
A-15	C	5500	2	2.62	357
A-16	C	2500	3	3.52	210
A-17	C	4000	3	3.32	237
A-18	C	5500	3	3.24	357
A-19	R	2500	1	1.75	228
A-20	R	4000	1	1.66	261
A-21	R	5500	1	1.35	264
A-22	R	2500	2	3.05	252
A-23	R	4000	2	2.31	201
A-24	R	5500	2	2.04	354
A-25	R	2500	3	3.92	246
A-26	R	4000	3	3.75	310
A-27	R	5500	3	3.6	378

Similarly, the value of magnetic flux density increased by the increasing the energy level. When capacitor bank discharged at the same level of energy and capacitance with three different cross-section shape of coils. The maximum magnetic flux density of 2.01 T was produced in the square coil with maximum discharge time of 225 μs, and the minimum flux density of 1.75 T produced in the rectangular coil with maximum discharge time of 228 μs Maximum discharge time increased with increasing capacitance. The maximum magnetic flux density of 3.64 T was observed in square cross-section coil at the 3-kJ energy level with capacitance of 2500 μF, and the minimum magnetic fluxed density of 1.35 T observed in rectangular cross-section shape of the coil on 1 kJ energy with capacitance of 5500 μF.

5.1.2 Lorentz Force Contribution

Lorentz force is related to the magnetic flux density, whose distribution mainly depends on the geometric structure of the coil cross-section.
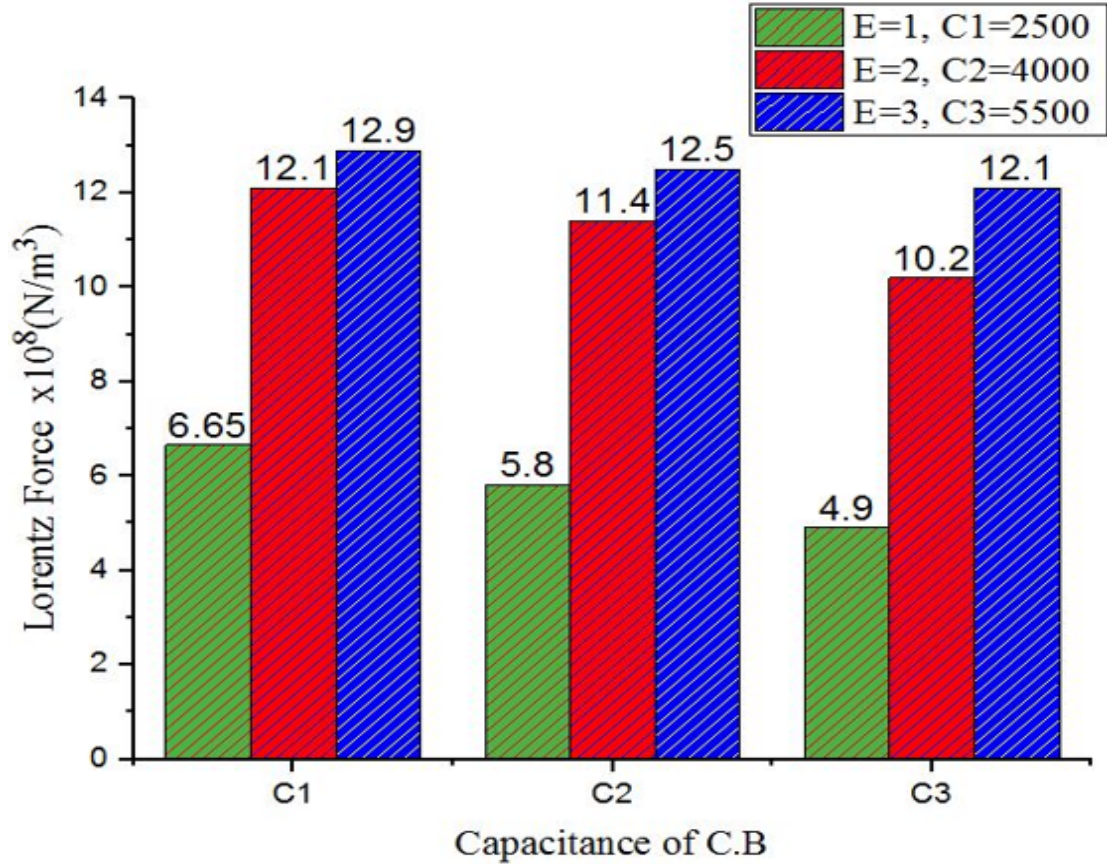
FIGURE 5.2: Maximum Lorentz force produced in different coils

C1 is the 2500 μF capacitance, C2 is the 4000 μF capacitance. C3 is the 5500 μF capacitance, E1 is the 1kJ energy level, E2 is the 2kJ energy level, E3 is the 3kJ energy level, and C.B is the capacitor bank.

Lorentz force of square coil at the different energy levels with different capacitance is shown in Figure 5.2. It is observed that Lorentz force decreased by increasing the capacitance with same energy level. For 1kJ, maximum Lorentz force of 665 MN/m3 is observed at 2500 μF capacitance, and a minimum of 490 MN/m3 was noticed at 5500 μF of capacitance. 12.78% increase was observed when changing the capacitance from 4000 μF to 2500μF, and 15.5% increase was observed when capacitance changed from 5500 μF to 4000 μF. Lorentz force in three different coils with different energy and capacitance levels is shown in **Table 5.2**.

TABLE 5.2: Magnetic flux density with respect to time

S. No	Coil cross-section shape	Capacitance (μF)	Energy Level (kJ)	Lorentz force × e8 N/m3	Time (μs)
A-1	S	2500	1	6.65	175
A-2	S	4000	1	5.8	196
A-3	S	5500	1	4.9	234
A-4	S	2500	2	12.1	160
A-5	S	4000	2	11.4	213
A-6	S	5500	2	10.2	237
A-7	S	2500	3	12.9	189
A-8	S	4000	3	12.5	220
A-9	S	5500	3	12.1	252
A-10	C	2500	1	5.85	195
A-11	C	4000	1	4.4	231
A-12	C	5500	1	3.6	252
A-13	C	2500	2	9.5	189
A-14	C	4000	2	8	210
A-15	C	5500	2	6.4	227
A-16	C	2500	3	10.9	180
A-17	C	4000	3	9.5	230
A-18	C	5500	3	8.6	250
A-19	R	2500	1	3.7	265
A-20	R	4000	1	2.9	216
A-21	R	5500	1	2.5	237
A-22	R	2500	2	11.6	190
A-23	R	4000	2	10.9	240
A-24	R	5500	2	10.02	250
A-25	R	2500	3	12.1	189
A-26	R	4000	3	11.4	220
A-27	R	5500	3	10.8	230

S is the square cross-section of the coil, C is the circular cross-section shape of the coil, R is the rectangular cross-section shape of the coil. It is observed that Lorentz force decreases by increasing the level of the capacitance, and increased by increasing the energy level from **Table 5.2**. The geometry of the coil also effects

the Lorenz force. The maximum Lorentz force is observed in the square coil and it is minimum in the rectangular cross-section shape of coil. The maximum Lorentz force of 12.9 x e08 N/m3 was observed in square cross-section coil at 3 kJ energy with 2500 μF capacitance. The minimum Lorentz force of 2.5 x e08 N/m3 was observed in the rectangular coil at the 1 kJ level energy with 5500 μF capacitance.

5.1.3 Discharge Current

The discharge current peak and its waveform depended on the energy level, capacitance and cross-section of the coil. **Figure 5.3**. shown the discharge current waveform at fixed energy and capacitance level for different cross-sections of the coils. It was observed that square coil produced maximum discharge current of 13.75 kA, and minimum of 12.3 kA discharge current developed in the rectangular coil.
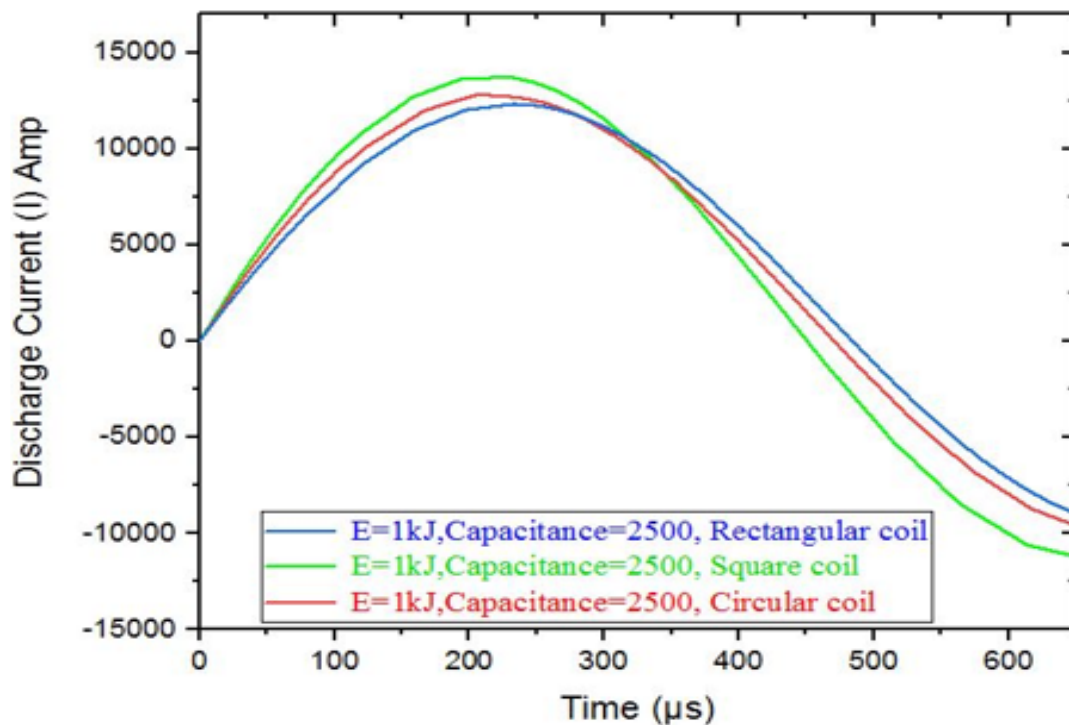
FIGURE 5.3: Current waveform on different cross-section shapes of the coil

C1 is the 2500μF capacitance, E1 is the 1 kJ energy, S is the square cross-section shape of the coil, C is the circular cross-section of the coil, R is the rectangular cross-section of the coil.

TABLE 5.3: The maximum peak current of numerically, experimental, time taken for peak current, and percentage error between numerical and experimental current

S. No	Coil cross-section	Capacitance	Energy Level	Numerical peak	Time	Experimental peak	Percentage
	shape	mu	(kJ)	Current (kA)	mu	Current (kA)	error
A-1	S	2500	1	13.75	210	15.1	2.48
A-2	S	4000	1	13.5	265	13.7	1.4
A-3	S	5500	1	13.1	330	13.2	0.75
A-4	S	2500	2	19.7	215	19.8	0.5
A-5	S	4000	2	18.8	265	19.2	2.08
A-6	S	5500	2	18.6	330	18.8	0.1
A-7	S	2500	3	23.1	226	23.9	2.9
A-8	S	4000	3	22.6	270	23	1.7
A-9	S	5500	3	22.2	320	22.8	2.6
A-10	C	2500	1	13.6	200	13.6	0
A-11	C	4000	1	13.2	275	13.2	0
A-12	C	5500	1	12.8	320	12.9	0.77
A-13	C	2500	2	19	210	18.8	1.05
A-14	C	4000	2	18.8	275	18.2	3.1
A-15	C	5500	2	17.8	320	18.1	1.65

Continued Table: 5.3 The maximum peak current of numerically, experimental, time taken for peak current, and percentage error between numerical and experimental current

S. No	Coil cross-section	Capacitance	Energy Level	Numerical peak	Time	Experimental peak	Percentage
	shape	mu	(kJ)	Current (kA)	mu	Current (kA)	error
A-16	C	2500	3	22.8	180	22.9	0.43
A-17	C	4000	3	22.5	270	21.9	2.67
A-18	C	5500	3	21.8	320	21.8	0
A-19	R	2500	1	12.3	210	12.3	0
A-20	R	4000	1	11.8	270	11.8	0
A-21	R	5500	1	11.5	320	11.5	0
A-22	R	2500	2	17	225	16.8	1.17
A-23	R	4000	2	16.7	280	16.6	0.59
A-24	R	5500	2	16	320	16.2	1.23
A-25	R	2500	3	20.8	230	20.4	1.9
A-26	R	4000	3	20	290	19.7	1.5
A-27	R	5500	3	19.5	350	19.6	0.51

5.2   Numerical Results of Solid Mechanics Model

The output of the electromagnetic model is used as an input of the solid mechanic's model. This section described the deformation contours of the aluminum worksheet, the height of the deformed workpiece, dome profile, and thickness variation of the deformed workpiece.

5.2.1 Deformation

The numerical deformation of the workpiece with respect to time is shown in **Figure 5.4**. The capacitor bank discharge at 1 kJ energy and 5500μF capacitance in the square cross-sectional area of the coil. The deformation of the workpiece started at 90 μs of discharge pulse. It started from center of coil.
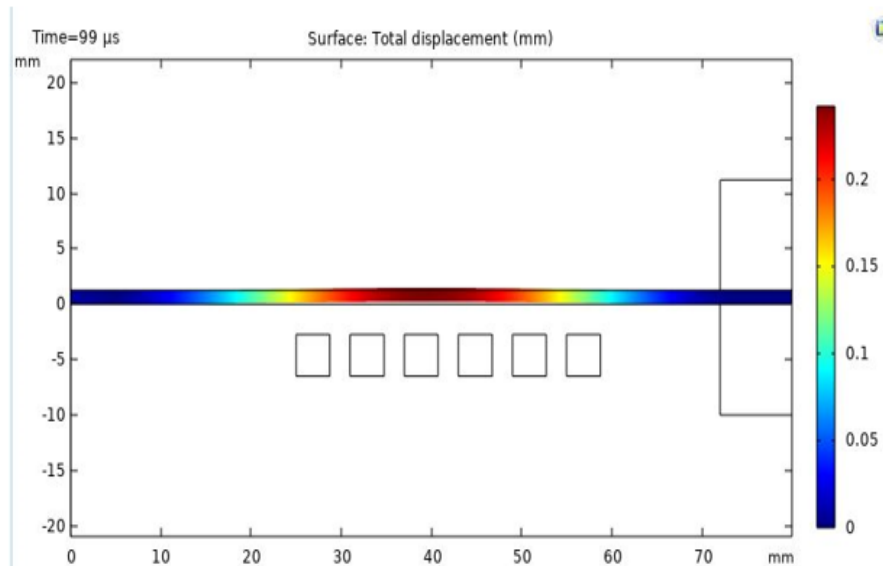
FIGURE 5.4: Deformation of the workpiece at 99 μs

The workpiece deformed only 0.25 mm after 99 μs. After 201 μs, the workpiece deformed 1.64 mm.
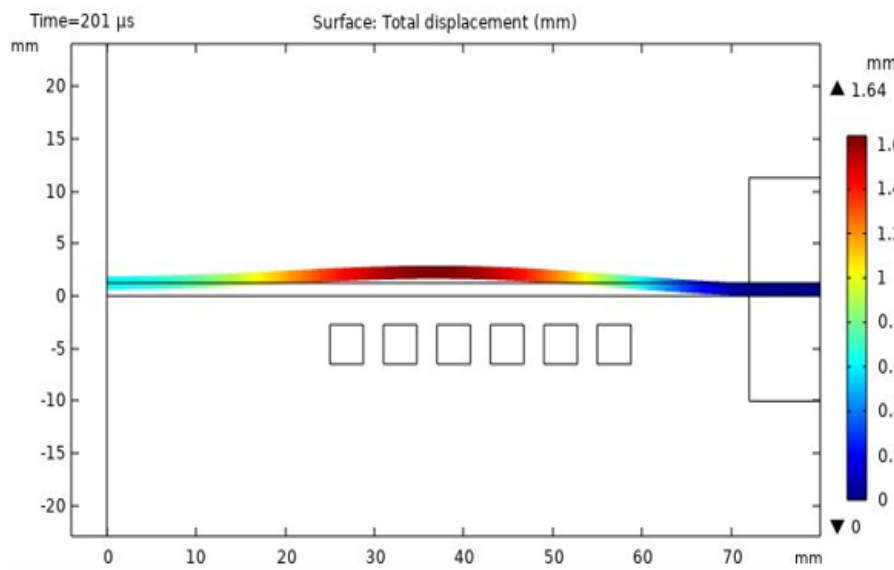
FIGURE 5.5: Deformation of the workpiece at 201 μs

The workpiece deformation started from the center of the sheet shown in figure 5.5. The workpiece that gained 5.18 height above the reference line is presented in **figure 5.6**. The contribution of the Lorentz force decreasing after 234 μs. But the workpiece deformation is continued due to the inertial effect of high velocity. Finally, the workpiece completely defoamed to maximum height at 390 μs shown in **figure 5.7**.
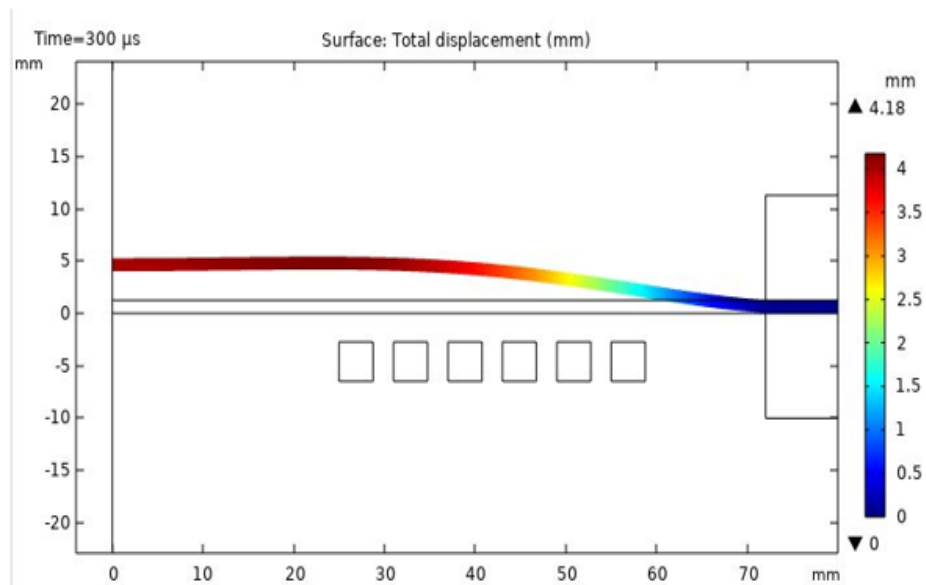
FIGURE 5.6: Deformation of workpiece at 300 μs
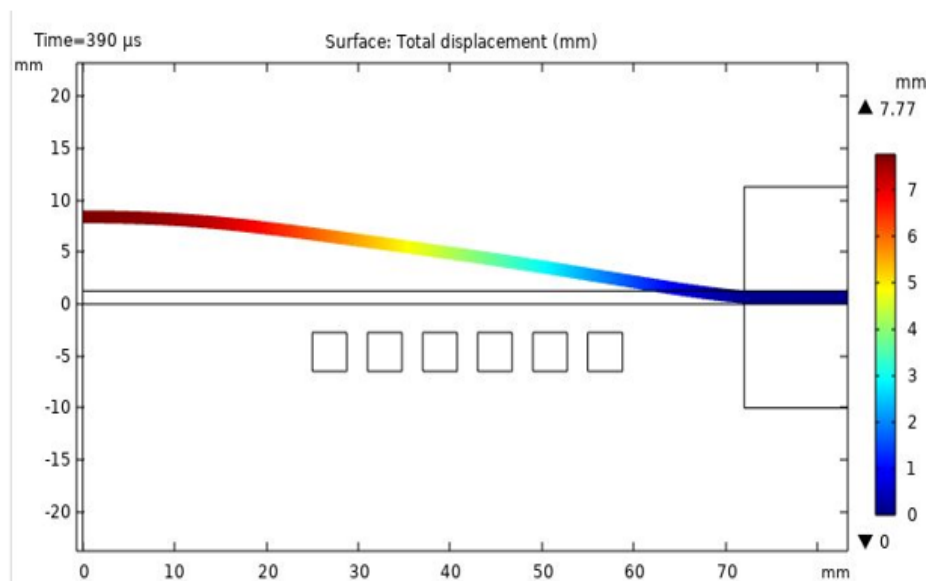
FIGURE 5.7: Deformation of workpiece at 330 μs

5.2.1.1 Dome Height and Profile Shape

The numerical deformation profile of the deformed workpiece is shown in **Figure 5.8**. The figure showed the comparison among the three different cross-sectional shapes of the coil at the same energy and capacitance level.

FIGURE 5.8: Comparison of a simulation dome shape and height

S is the square cross-section of the coil, C Is the circular cross-section of the coil, R is the rectangular cross-section shape of the coil, C1 is 2500 μF capacitance, E3 is 3 kJ energy.

Dome height of Square cross-section is greater than other cross-section at same process parameters. Dome heights for all simulations are summarized in **Table 5.4**.

TABLE 5.4: Dome height of simulation

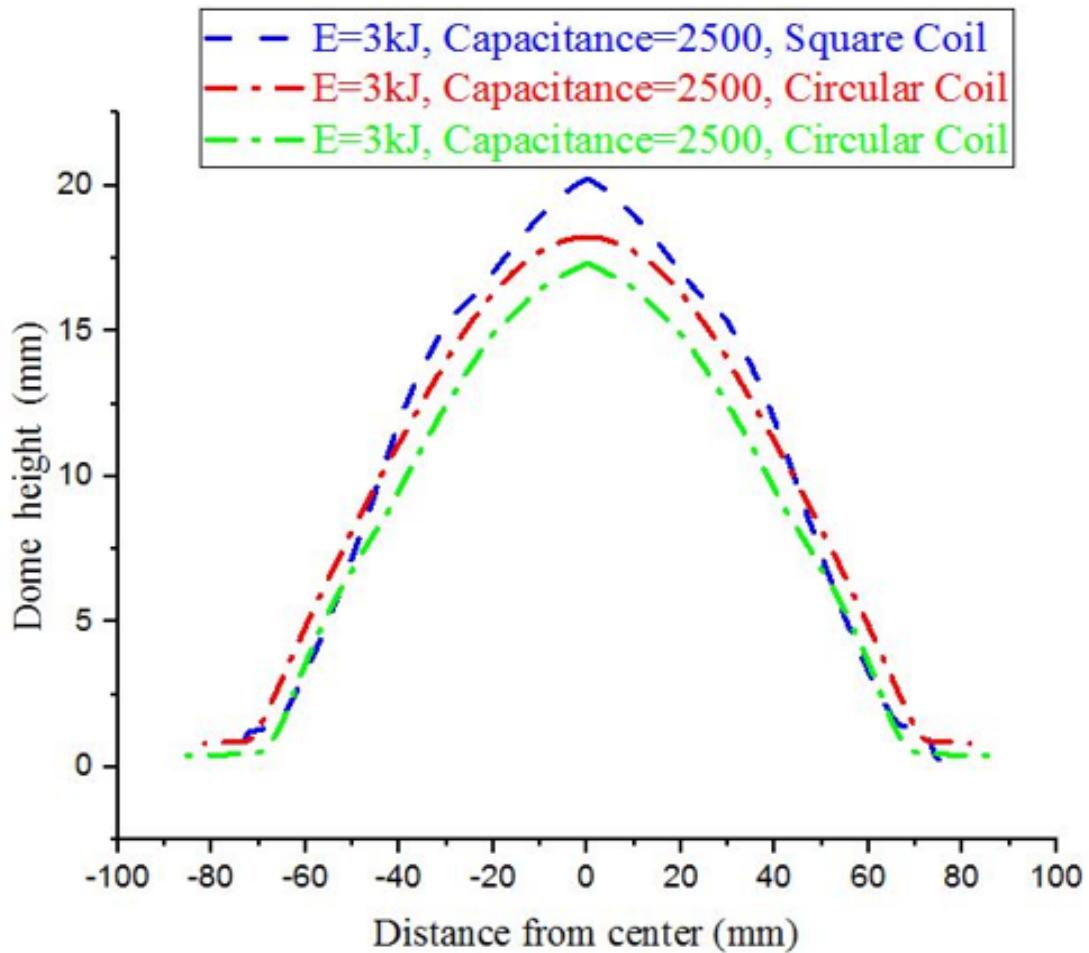| S. No	Coil cross-section shape	Capacitance (μF)	Energy Level (kJ)	Dome height (mm)
A-1	S	2500	1	8.7758
A-2	S	4000	1	7.7707
A-3	S	5500	1	7.0886
A-4	S	2500	2	18.368
A-5	S	4000	2	15.94
A-6	S	5500	2	12.571
A-7	S	2500	3	20.226
A-8	S	4000	3	19.282
A-9	S	5500	3	18.526
A-10	C	2500	1	8.7929
A-11	C	4000	1	8.6523
A-12	C	5500	1	6.7783
A-13	C	2500	2	14.086
A-14	C	4000	2	11.046
A-15	C	5500	2	9.117
A-16	C	2500	3	18.227
A-17	C	4000	3	16.572
A-18	C	5500	3	14.657
A-19	R	2500	1	6.3067
A-20	R	4000	1	5.6496
A-21	R	5500	1	5.5423
A-22	R	2500	2	12.215
A-23	R	4000	2	11.565
A-24	R	5500	2	11.344
A-25	R	2500	3	17.319
A-26	R	4000	3	15.624
A-27	R	5500	3	12.288

Table 5.4 shows that the square coil with 2500 μF capacitance and 3 kJ energy level obtained maximum dome height. It is also observed that the dome height increased by increasing the energy level, and it is decreased by increasing the capacitance of capacitor bank

5.2.1.2 Thickness Distribution

When the work piece gets deformed, the distribution along the radial direction of the aluminum sheet was observed. The maximum thickness reduction has occurred at the center of the deformed workpiece. This phenomenon happens due to the inertial effect during the deformation process. The numerical comparison of reduction in thickness for square and rectangular cross-section is shown in **Figure 5.9**.

Maximum thickness reduction at the point of maximum dome height in both cases were observed. Maximum thickness reduction is observed when the workpiece deformed through the square coil with 2500 μF and 3 kJ energy, and minimum thickness reduction measured in the workpiece which is deformed through rectangular cross section shape of coil at 1 kJ energy and 5500 μF of capacitor bank.
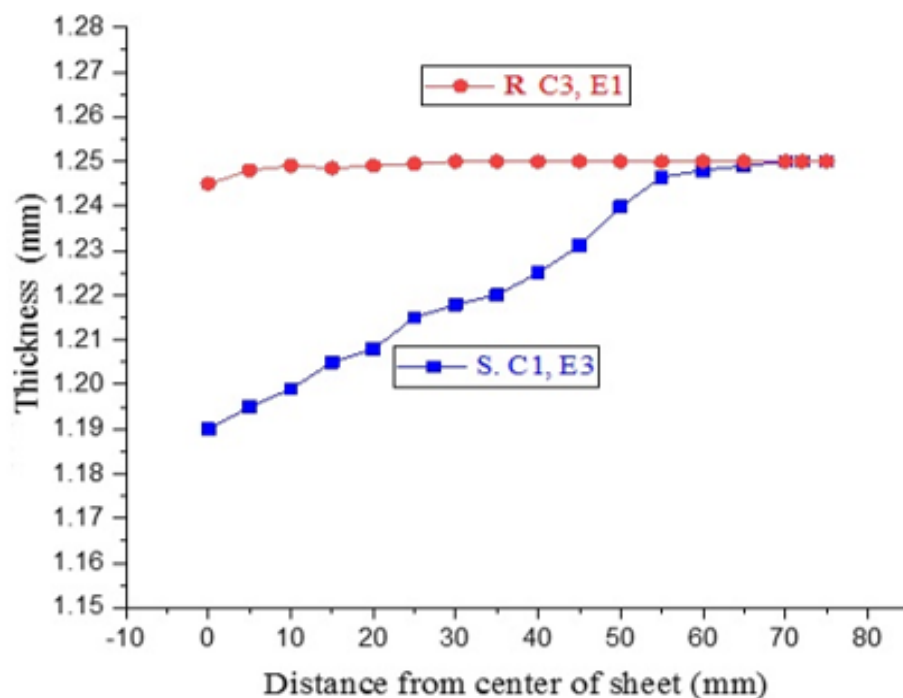

FIGURE 5.9: Thickness distribution in the best and worst sample

Where, R is the rectangular cross section of coil, C3 is the 5500 μF capacitance, E1 is the 1kJ energy, S is the square cross section of coil, C1 is the 2500 μF capacitance, and E3 is the 3 kJ energy level

5.3 Comparison and Validation

The numerical model validated with experimental result. The comparison between experimental discharge current and current observed in numerical model is shown in **Figure 5.10**. The percentage errors in experimental and simulation values of maximum, minimum, and average current responses are 3.35%, 0.8% and 1.6% respectively. Previous studies [18]. [64] have shown similar trends.
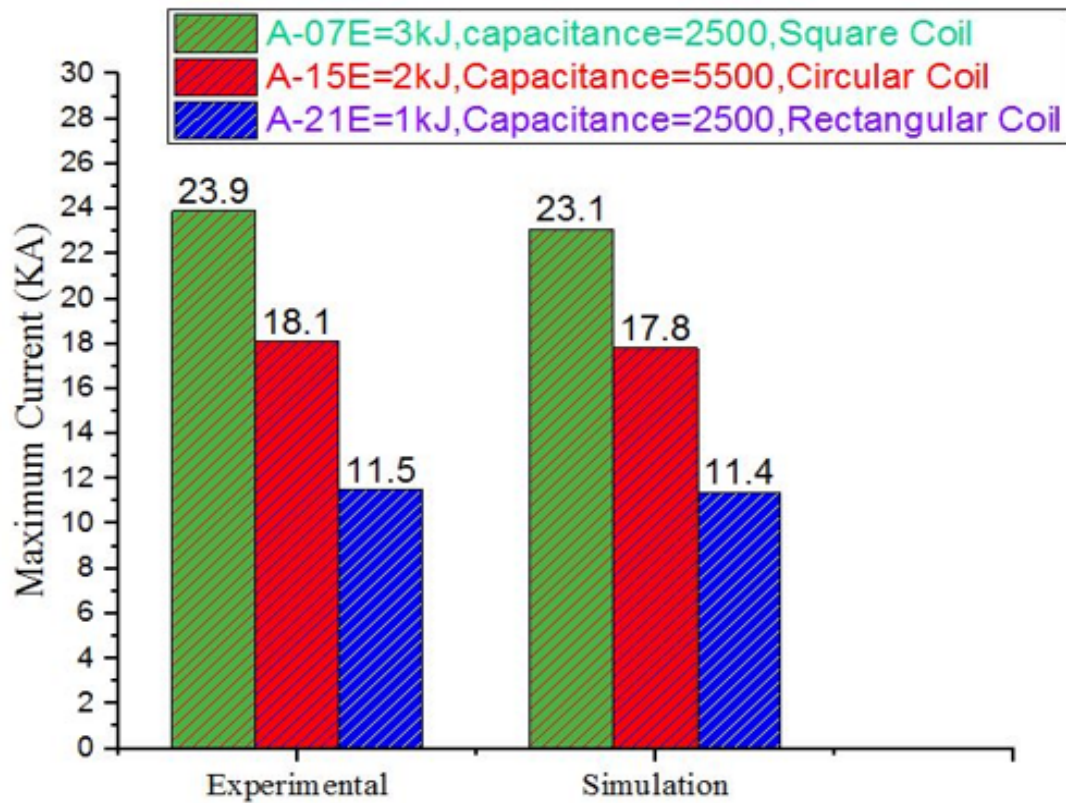

FIGURE 5.10: The maximum current peak in Best, worst, and Average discharging.

A-07, A-15, and A-21 are best, optimum, and worst experiments. A-07 (Coil cross section is square, E= 3kJ, Capacitance = 2500 μF), A-15 (Coil cross section is circular, E= 3kJ, Capacitance = 5500 μF), and A-21 (Coil cross section is square, E= 1kJ, Capacitance = 5500 μF).

5.3.1 Axial Deformation and Profile Shape

The maximum Dome height was measured 20.6215 mm experimental and 20.226 by numerically. the percentage error in axial deformation is 1.92% which was allow for experimental work. The Dome height was depended on the selected variables. **Figure No 5.11** was shown the maximum Dome height varied to energy level, capacitance, and coil cross section shape. The Maximum Dome height was increased by increasing the energy level of capacitor bank. this is good agreement with previous research [32].

the Dome height was increased by decreasing the capacitance of the capacitor bank. if the capacitance of capacitor bank was too low or too high, decreased the Dome height[18]. The grater Dome height was observed in square cross section shape of coil comparative to other cross section shape of coil. The square coil has generate the more magnetic field which is cause of greater axial deformation [60]. The numerical results are validate with experimental result.
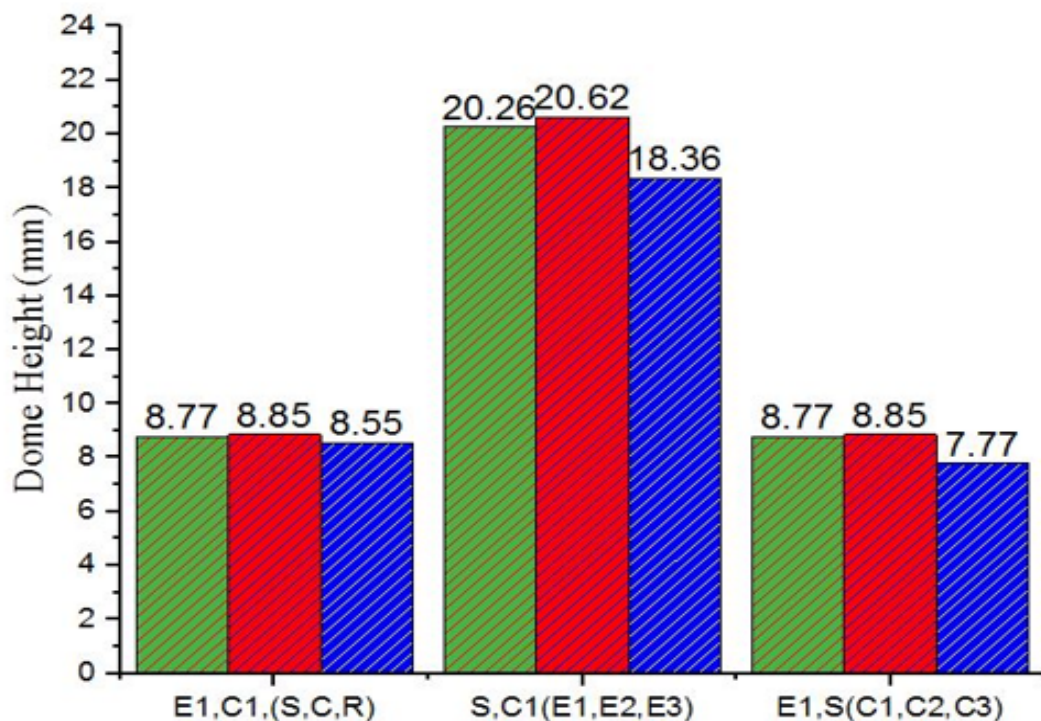
FIGURE 5.11: The maximum Dome height

E1 is the 1kJ energy, E2 is the 2 kJ, E3 is the 3kJ energy. S is the square coil, R is the rectangular coil, C is the circular coil, C1 is the 2500μF, C2 is the 4000μF, and C3 is the 5500μF.

5.3.2 Profile Shape of Deformation

Figure 5.12 shown the comparison of experimental and numerical result of dome shape profile for circular cross-section coil at 3kJ energy and 5500 μF capacitance. Error bars were drawn on the basis of three sets of experiments. The numerical result falls within error bar of experimental results. Actual and Numerical deformation of work piece is shown in **Figure 5.13 & (5.14)**.

FIGURE 5.12: Comparison between experimental and numerical deformation
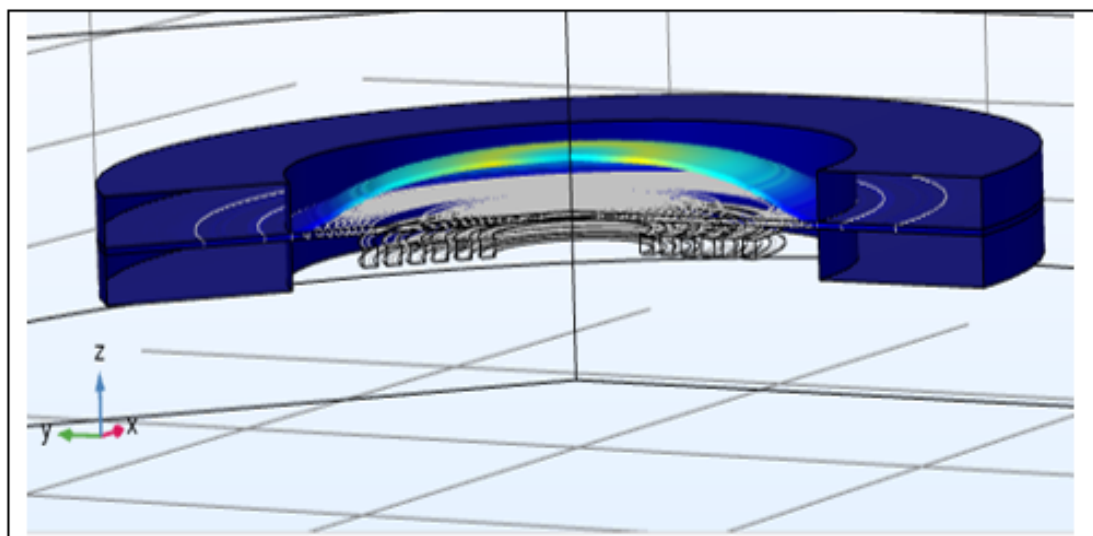
FIGURE 5.13: 3D Numerical deformation
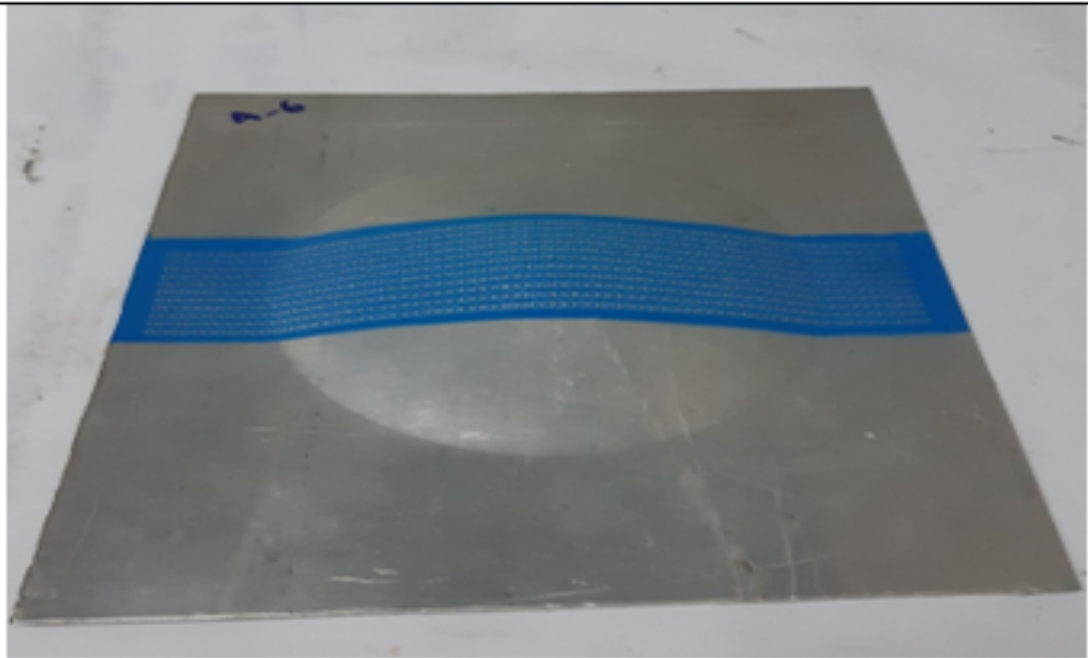
FIGURE 5.14: Experimental Deformation

Chapter 6

Conclusion and Future Work

6.1   Conclusions

Electromagnetic forming process for free forming of AL 6061-T6 alloy sheets was analyzed in the present work. The experim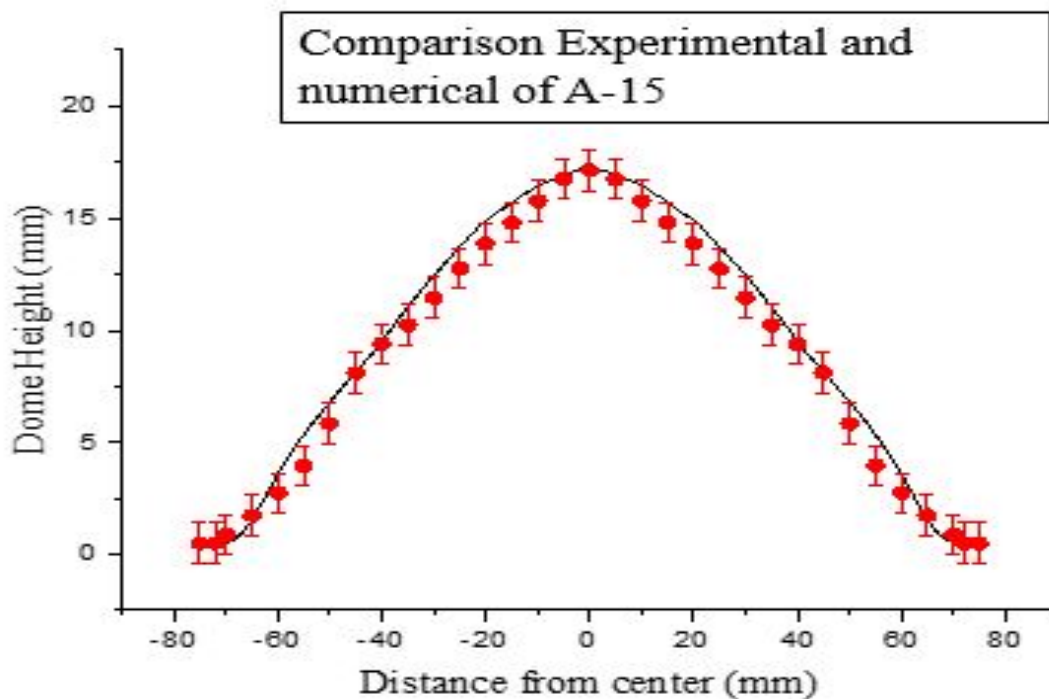ental data was analyzed with ANOVA and main effect plots. Fully coupled finite element model was also developed and validated against experimental results. Following important conclusions can be drawn from this work:

1. The maximum Dome height in workpiece was observed at 3 kJ energy, 2500 μF capacitance, and square cross section of actuator coil.

2. The minimum Dome height in workpiece was observed at 1 kJ energy, 5500 μF capacitance, and rectangular cross section of actuator coil.

3. The minimum thickness variation in the deformed workpiece was observed at 1 kJ energy, 5500 μF capacitance and rectangular cross section of actuator coil.

4. The maximum thickness variation in the deformed workpiece was observed at 3 kJ energy, 2500 μF capacitance, and square cross section of actuator coil.

5. Energy level of the capacitor is the most statistically significant for Dome height and thickness variation having a contribution ratio of 79

75

6. The minimum thickness was measured in region B, 15 mm away from sheet centre. The maximum thickness was observed in region A (top centre of the dome).

7. The elongation in sheet work piece was analyzed by using the optical microscope. Elongation in the radial and transvers direction was measured 6.7

8. Numerically obtained results were compared against experimental results and an error around 5

6.2 Future Work

Following future research avenues have been identified in this research:

1. The presented research work can be extended toward closed-die forming of simple and complex shapes.

2. The conflicting nature of process parameter observed for Dome height and thickness variation shows that there is a need of multi-objective optimization in EMF process.

3. The wok presented in this research can be extended to the sheets of other alloys.

Bibliography

[1] S. Kalpakjian and S. R. Schmid, *Manufacturing Engineering and Technology*. Pearson Education, Limited, 2013.

[2] M. Groover, *Fundamentals of Modern Manufacturing: Materials, Processes, and Systems*, 4th editio. John Wiley & Sons, Inc., 2010.

[3] M. L. Bohn, S. G. Xu, K. J. Weinmann, C. C. Chen, and A. Chandra, "Improving formability in sheet metal stamping with active drawbead technology," *J. Eng. Mater. Technol. Trans. ASME*, vol. 123, no. 4, pp. 504–510, 2001, doi: 10.1115/1.1395577.

[4] J. T. Black and R. A. Kohser, *DeGarmo's Materials and Processes in Manufacturing*, 10th ed. John Wiley & Sons, Inc, 2008.

[5] D. Li and A. K. Ghosh, "Biaxial warm forming behavior of aluminum sheet alloys," *J. Mater. Process. Technol.*, vol. 145, no. 3, pp. 281–293, 2004, doi: 10.1016/j.jmatprotec.2003.07.003.

[6] H. C. Shih and W. R. D. Wilson, "Effects of contact pressure and strain on friction in sheet-metal forming©," *Tribol. Trans.*, vol. 42, no. 1, pp. 144–151, 1999, doi: 10.1080/10402009908982201.

[7] C. W. Hsu, A. G. Ulsoy, and M. Y. Demeri, "An approach for modeling sheet metal forming for process controller design," *J. Manuf. Sci. Eng. Trans. ASME*, vol. 122, no. 4, pp. 717–724, 2000, doi: 10.1115/1.1286815.

[8] V. S. B. and G. S. Daehn, "Hyperplasticity: increased forming limits at high workpiece velocityv," *Endocrinol. Metab. Clin. North Am.*, vol. 23(3), no. Physiology of the hypothalamic-pituitary-adrenal axis in health and dysregulation in psychiatric and autoimmune disorders., pp. 451–466, 1994.

[9] M. Seth, V. J. Vohnout, and G. S. Daehn, "Formability of steel sheet in high velocity impact," *J. Mater. Process. Technol.*, vol. 168, no. 3, pp. 390–400, 2005, doi: 10.1016/j.jmatprotec.2004.08.032.

[10] E. Sugawara and H. Nikaido, "Properties of AdeABC and AdeIJK efflux systems of Acinetobacter baumannii compared with those of the AcrAB-TolC system of Escherichia coli," *Antimicrob. Agents Chemother*, vol. 58, no. 12, pp. 7250–7257, 2014, doi: 10.1128/AAC.03728-14.

[11] V. S. Balanethiram and G. S. Daehn, "Enhanced formability of interstitial free iron at high strain rates," *Scr. Metall. Mater.*, vol. 27, no. 12, pp. 1783–1788, 1992, doi: 10.1016/0956-716X(92)90019-B.

[12] C. Zener and J. H. Hollomon, "Effect of strain rate upon plastic flow of steel," J. Appl. Phys., vol. 15, no. 1, pp. 22–32, 1944, doi: 10.1063/1.1707363.

[13] E. Iriondo, M. A. Gutiérrez, B. González, J. L. Alcaraz, and G. S. Daehn, "Electromagnetic

impulse calibration of high strength sheet metal structures," *J. Mater. Process. Technol.*, vol. 211, no. 5, pp. 909–915, 2011.

[14] S. Akbar, M. S. Awan, M. A. Aleem, M. N. Sarwar, and M. Farooque, "Effect of Field Intensity on Electromagnetic Flat Sheet Forming," in *Materials Today: Proceedings*, 2015, vol. 2, no. 10, pp. 5324–5328.

[15] X. Zhang, Z. R. Wang, F. M. Song, L. Z. Yu, and X. Lu, "Finite element simulation of the electromagnetic piercing of sheet metal," *J. Mater. Process. Technol.*, vol. 151, no. 1-3 SPEC. ISS., pp. 350–354, 2004, doi: 10.1016/j.jmatprotec.2004.04.086.

[16] Y. B. Park, H. Y. Kim, and S. I. Oh, "Design of axial/torque joint made by electromagnetic forming," *Thin-Walled Struct.*, vol. 43, no. 5, pp. 826–844, 2005, doi: 10.1016/j.tws.2004.10.009.

[17] S. D. Kore, P. P. Date, and S. V. Kulkarni, "Effect of process parameters on electromagnetic impact welding of aluminum sheets," *Int. J. Impact Eng.*, vol. 34, no. 8, pp. 1327–1341, 2007, doi: 10.1016/j.ijimpeng.2006.08.006.

[18] Q. Cao et al., "Effects of current frequency on electromagnetic sheet metal forming process," *IEEE Trans. Appl. Supercond.*, vol. 24, no. 3, 2014, doi: 10.1109/TASC.2013.2279886.

[19] H. Ma, L. Huang, J. Li, X. Duan, and F. Ma, "Effects of process parameters on electromagnetic sheet free forming of aluminium alloy," *Int. J. Adv. Manuf. Technol.*, vol. 96, no. 1–4, pp. 359–369, 2018, doi: 10.1007/s00170-018-1589-6.

[20] W. Xiao, L. Huang, J. Li, H. Su, F. Feng, and F. Ma, "Investigation of spring-back during electromagnetic-assisted bending of aluminium alloy sheet," Int. J. Adv. Manuf. Technol, vol. 105, no. 1-4, pp. 375–394, 2019.

[21] M. Kamal and G. S. Daehn, "A uniform pressure electromagnetic actuator for forming flat sheets," *J. Manuf. Sci. Eng. Trans. ASME*, vol. 129, no. 2, pp. 369–379, 2007, doi: 10.1115/1.2515481.

[22] S. T. S. Al-Hassani, J. L. Duncan, and W. Johnson, *The Influence of the Electrical and Geometrical Parameters in Magnetic Forming.* Pergamon Press Ltd., 1968.

[23] N. Takatsa, M. Kato, K. Sato, and T. Tobe, "High-speed forming of metal sheets by electromagnetic force.," *JSME Int. journal. Ser. 3, Vib. Control Eng. Eng. Ind.*, vol. 31, no. 1, pp. 142–148, 1988, doi: 10.1299/jsmec1988.31.142.

[24] G. K. Fenton and G. S. Daehn, "Modeling of electromagnetically formed sheet metal," *J. Mater. Process. Technol.*, vol. 75, no. 1–3, pp. 6–16, 1998, doi: 10.1016/S0924-0136(97)00287-2.

[25] L. Wang, Z. Y. Chen, C. X. Li, and S. Y. Huang, "Numerical simulation of the electromagnetic sheet metal bulging process," *Int. J. Adv. Manuf. Technol.*, vol. 30, no. 5–6, pp. 395–400, Sep. 2006, doi: 10.1007/s00170-005-0094-x.

[26] J. P. M. Correia, M. A. Siddiqui, S. Ahzi, S. Belouettar, and R. Davies, "A simple model to simulate electromagnetic sheet free bulging process," *Int. J. Mech. Sci.*, vol. 50, no. 10–11, pp. 1466–1475, 2008,

[27] D. Xu, X. Liu, K. Fang, and H. Fang, "Calculation of electromagnetic force in electromagnetic forming process of metal sheet," *J. Appl. Phys.*, vol. 107, no. 12, 2010, doi: 10.1063/1.3437201.

[28] N. Liu et al., "A comparative study on the effects of boundary constraints on electromagnetic sheet forming," *Int. J. Adv. Manuf. Technol.*, vol. 101, no. 9–12, pp. 2785–2793, 2019, doi: 10.1007/s00170-018-3098-z.

[29] X. Cui, J. Li, J. Mo, J. Fang, B. Zhou, and X. Xiao, "Effect of the sheet thickness and current damping exponent on the optimum current frequency in electromagnetic forming," *Int. J. Adv. Manuf. Technol.*, vol. 85, no. 1–4, pp. 843–851, 2016, doi: 10.1007/s00170-015-7983-4.

[30] J. M. Imbert, S. L. Winkler, M. J. Worswick, D. A. Oliveira, and S. Golovashchenko, "The effect of tool-sheet interaction on damage evolution in electromagnetic forming of aluminum alloy sheet," *J. Eng. Mater. Technol. Trans. ASME*, vol. 127, no. 1, pp. 145–153, 2005, doi: 10.1115/1.1839212.

[31] M. Padmanabhan, "Wringkling and springback in electromagnetic sheet metal forming and electromagnetic ring compression (Doctoral dissertation)." pp. 1–205, 1997, Accessed: Jan. 22, 2021.

[32] D. A. Oliveira, M. J. Worswick, M. Finn, and D. Newman, "Electromagnetic forming of aluminum alloy sheet: Free-form and cavity fill experiments and model," *J. Mater. Process. Technol.*, vol. 170, no. 1–2, pp. 350–362, Dec. 2005, doi: 10.1016/j.jmatprotec.2005.04.118.

[33] E. Paese, M. Geier, R. P. Homrich, and J. L. Pacheco, "Simplified mathematical modeling for an electromagnetic forming system with flat spiral coil as actuator," *J. Brazilian Soc. Mech. Sci. Eng.*, vol. 33, no. 3, pp. 324–331, 2011, doi: 10.1590/S1678-58782011000300008.

[34] E. Paese, P. A. R. Rosa, M. Geier, R. P. Homrich, and R. Rossi, "An analysis of electromagnetic sheet metal forming process," *Appl. Mech. Mater.*, vol. 526, pp. 9–14, 2014, doi: 10.4028/www.scientific.net/AMM.526.9.

[35] E. Paese, M. Geier, R. P. Homrich, P. Rosa, and R. Rossi, "Sheet metal electromagnetic forming using a flat spiral coil: Experiments, modeling, and

validation," *J. Mater. Process. Technol.*, vol. 263, pp. 408–422, 2019, doi: 10.1016/j.jmatprotec.2018.08.033.

[36] A. El-Azab, M. Garnich, and A. Kapoor, "Modeling of the electromagnetic forming of sheet metals: State-of-the-art and future needs," *J. Mater. Process. Technol.*, vol. 142, no. 3, pp. 744–754, 2003, doi: 10.1016/S0924-0136(03)00615-0.

[37] J. Jablonski and R. Winkler, "Analysis of the electromagnetic forming process," *Int. J. Mech. Sci.*, vol. 20, no. 5, pp. 315–325, 1978, doi: 10.1016/0020-7403(78)90093-0.

[38] W. H. Gourdin, "Analysis and assessment of electromagnetic ring expansion as a high-strain-rate test," *J. Appl. Phys.*, vol. 65, no. 2, pp. 411–422, 1989, doi: 10.1063/1.343121.

[39] P. L'Eplattenier, G. Cook, C. Ashcraft, M. Burger, J. Imbert, and M. Worswick, "Introduction of an electromagnetism module in LS-DYNA for coupled mechanical-thermal-electromagnetic simulations," *Steel Res. Int.*, vol. 80, no. 5, pp. 351–358, 2009, doi: 10.2374/SRI08SP152.

[40] A. L. Gurson, "Continuum theory of ductile rupture by void nucleation and growth," *J. Eng. Mater. Technol.*, vol. 99, no. 76, pp. 2–15, 1977.

[41] V. Tvergaard, "Influence of voids on shear band instabilities under plane strain conditions," *Int. J. Fract.*, vol. 17, no. 4, pp. 389–407, 1981, doi: 10.1007/BF00036191.

[42] V. Tvergaard and A. Needleman, "Analysis of the cup-cone fracture in a round tensile bar," *Acta Metall.*, vol. 32, no. 1, pp. 157–169, 1984, doi: 10.1016/0001-6160(84)90213-X.

[43] M. A. Siddiquei, "Numerical Modelling and Simulation of Electromagnetic Forming Process," p. 214, 2009.

[44] A. H. Meriched, M. Féliachi, and H. Mohellebi, "Electromagnetic Forming of Thin Metal Sheets," *IEEE Trans. Magn.*, vol. 36, no. 4 PART 1, pp. 1804–1807, 2000, doi: 10.1109/20.877795.

[45] J. Unger, M. Stiemer, B. Svendsen, and H. Blum, "Multifield modeling of electromagnetic metal forming processes," J. Mater. Process. *Technol.*, vol. 177, no. 1–3, pp. 270–273, 2006, doi: 10.1016/j.jmatprotec.2006.03.190.

[46] J. J. M. S. I. Boyd, "Increased formability and the effects of the tool/sheet interaction in electromagnetic forming of aluminum alloy sheet," 2005.

[47] J. P. M. Correia, M. A. Siddiqui, S. Ahzi, S. Belouettar, and R. Davies, "A simple model to simulate electromagnetic sheet free bulging process," *Int. J. Mech. Sci.*, vol. 50, no. 10–11, pp. 1466–1475, Oct. 2008, doi: 10.1016/j.ijmecsci.2008.08.008.

[48] W. Luo, L. Huang, J. Li, X. Liu, and Z. Wang, "A novel multi-layer coil for a large and thick-walled component by electromagnetic forming," *J. Mater. Process. Technol.*, vol. 214, no. 11, pp. 2811–2819, 2014.

[49] E. Paese, M. Geier, R. P. Homrich, and R. Rossi, "A coupled electric-magnetic numerical procedure for determining the electromagnetic force from the interaction of thin metal sheets and spiral coils in the electromagnetic forming process," *Appl. Math. Model.*, vol. 39, no. 1, pp. 309–321, 2015, doi: 10.1016/j.apm.2014.05.032.

[50] Q. Cao et al., "Analysis and reduction of coil temperature rise in electromagnetic forming," *J. Mater. Process. Technol.*, vol. 225, pp. 185–194, Jun. 2015, doi: 10.1016/j.jmatprotec.2015.02.006.

[51] Z. Lai et al., "Investigation on plastic deformation behavior of sheet workpiece during radial Lorentz force augmented deep drawing process," *J. Mater. Process. Technol.*, vol. 245, pp. 193–206, Jul. 2017.

[52] Q. Cao et al., "Electromagnetic attractive forming of sheet metals by means of a dual-frequency discharge current: design and implementation," *Int. J. Adv. Manuf. Technol.*, vol. 90, no. 1–4, pp. 309–316, Apr. 2017, doi: 10.1007/s00170-016-9329-2.

[53] N. Takatsu et al., "Application of a uniform pressure actuator for electromagnetic processing of sheet metal," *Int. J. Adv. Manuf. Technol.*, vol. 36, no. 1, pp. 1804–1807, 2019, doi: 10.1109/20.877795.

[54] Z. Khan, M. Khan, S. H. Imran Jaffery, M. Younas, K. S. Afaq, and M. A. Khan, "Numerical and experimental investigation of the effect of process parameters on sheet deformation during the electromagnetic forming of AA6061-T6 alloy," *Mech. Sci.*, vol. 11, no. 2, pp. 329–347, 2020, doi: 10.5194/ms-11-329-2020.

[55] V. K. Barnwal, A. Tewari, K. Narasimhan, and S. K. Mishra, "Effect of plastic anisotropy on forming behavior of AA-6061 aluminum alloy sheet," *J. Strain Anal. Eng. Des.*, vol. 51, no. 7, pp. 507–517, 2016.

[56] D. Gayakwad, M. K. Dargar, P. K. Sharma, R. purohit, and R. S. Rana, "A Review on Electromagnetic Forming Process," *Procedia Mater. Sci.*, 2014, doi: 10.1016/j.mspro.2014.07.066.

[57] V. Psyk, D. Risch, B. L. Kinsey, A. E. Tekkaya, and M. Kleiner, "Electromagnetic forming - A review," *J. Mater. Process. Technol.*, 2011, doi: 10.1016/j.jmatprotec.2010.12.012.

[58] H. G. Noh, K. Lee, B. S. Kang, and J. Kim, "Inverse parameter estimation of the Cowper-Symonds material model for electromagnetic free bulge forming," *Int. J. Precis. Eng. Manuf.*, vol. 17, no. 11, pp. 1483–1492, Nov. 2016, doi: 10.1007/s12541-016-0174-x.

[59] Y. B. Guo, Q. Wen, and M. F. Horstemeyer, "An internal state variable plasticity-based approach to determine dynamic loading history effects on material property in manufacturing processes," *Int. J. Mech. Sci.*, vol. 47, no. 9, pp. 1423–1441, 2005, doi: 10.1016/j.ijmecsci.2005.04.015.

[60] S. Akbar, M. A. Aleem, F. Pirandad, M. S. Awan, S. Akhtar, and A. Haider, "Strip Size Optimization for Spiral Type Actuator Coil used in Electromagnetic Flat Sheet Forming Experiment," vol. 875, p. 9034112, 2021, doi: 10.4028/www.scientific.net/KEM.875.35.

[61] N. Liu et al., "Effects of the inner/outer diameters of flat spiral coils on electromagnetic sheet metal formation," *Int. J. Adv. Manuf. Technol.*, vol. 109, no. 5–6, pp. 1541–1551, 2020, doi: 10.1007/s00170-020-05729-5.

[62] J. Boyd, "Increased formability and the effects of the tool/sheet interaction in electromagnetic forming of aluminum alloy sheet," 2005.

[63] X. Cui, J. Mo, J. Fang, J. Li, Y. Zhu, and K. Zhong, "Variation of thickness distribution during electromagnetic sheet bulging," *Int. J. Adv. Manuf. Technol.*, vol. 80, no. 1–4, pp. 515–521, Sep. 2015, doi: 10.1007/s00170-015-7008-3.

[64] A. Shrivastava, A. Telang, A. K. Jha, and M. Ahmed, "Effect of thickness and energy on electromagnetic compression of AA6061 tube," *J. Brazilian Soc. Mech. Sci. Eng.*, vol. 42, no. 7, Jul. 2020, doi: 10.1007/s40430-020-02456-6.